

Search for Scalar Top and Scalar Bottom Quarks at $\sqrt{s} = 183$ GeV at LEP

The OPAL Collaboration

Abstract

Searches for a scalar top quark and a scalar bottom quark have been performed using a total data sample of 56.8 pb^{-1} at a centre-of-mass energy of $\sqrt{s} = 183$ GeV collected with the OPAL detector at LEP. No candidate events were observed. Combining this result with those obtained at lower centre-of-mass energies, the 95% C.L. lower limit on the scalar top quark mass is 85.0 GeV if the mixing angle between the supersymmetric partners of the left- and right-handed states of the top quark is zero. The lower limit is 81.3 GeV, even if the scalar top quark decouples from the Z^0 boson. These limits were obtained assuming that the scalar top quark decays into a charm quark and the lightest neutralino, and that the mass difference between the scalar top quark and the lightest neutralino is larger than 10 GeV. The complementary decay mode of the scalar top quark in which it decays into a bottom quark, a charged lepton and a scalar neutrino was also studied. From a similar analysis, a mass limit on the light scalar bottom quark was set at 82.7 GeV for a mass difference between the scalar bottom quark and the lightest neutralino larger than 7 GeV, and at 84.0 GeV for the mass difference larger 10 GeV and the lightest neutralino heavier than 30 GeV. These limits were obtained assuming that the scalar bottom quark decays into a bottom quark and the lightest neutralino, and that a mixing angle between the supersymmetric partners of the left- and right-handed states of the bottom quark is zero.

(To be submitted to Euro. Phys. J. C)

The OPAL Collaboration

K. Ackerstaff⁸, G. Alexander²³, J. Allison¹⁶, N. Altekamp⁵, K.J. Anderson⁹, S. Anderson¹²,
 S. Arcelli², S. Asai²⁴, D. Axen²⁹, G. Azuelos^{18,a}, A.H. Ball¹⁷, E. Barberio⁸, R.J. Barlow¹⁶,
 R. Bartoldus³, J.R. Batley⁵, S. Baumann³, J. Bechtluft¹⁴, C. Beeston¹⁶, T. Behnke⁸, A.N. Bell¹,
 K.W. Bell²⁰, G. Bella²³, S. Bentvelsen⁸, S. Bethke¹⁴, O. Biebel¹⁴, A. Biguzzi⁵, S.D. Bird¹⁶,
 V. Blobel²⁷, I.J. Bloodworth¹, J.E. Bloomer¹, M. Bobinski¹⁰, P. Bock¹¹, D. Bonacorsi²,
 M. Boutemour³⁴, B.T. Bouwens¹², S. Braibant¹², L. Brigliadori², R.M. Brown²⁰,
 H.J. Burckhart⁸, C. Burgard⁸, R. Bürgin¹⁰, P. Capiluppi², R.K. Carnegie⁶, A.A. Carter¹³,
 J.R. Carter⁵, C.Y. Chang¹⁷, D.G. Charlton^{1,b}, D. Chrisman⁴, P.E.L. Clarke¹⁵, I. Cohen²³,
 J.E. Conboy¹⁵, O.C. Cooke⁸, M. Cuffiani², S. Dado²², C. Dallapiccola¹⁷, G.M. Dallavalle²,
 R. Davis³⁰, S. De Jong¹², L.A. del Pozo⁴, K. Desch³, B. Dienes^{33,d}, M.S. Dixit⁷, E. do Couto e
 Silva¹², M. Doucet¹⁸, E. Duchovni²⁶, G. Duckeck³⁴, I.P. Duerdoth¹⁶, D. Eatough¹⁶,
 J.E.G. Edwards¹⁶, P.G. Estabrooks⁶, H.G. Evans⁹, M. Evans¹³, F. Fabbri², M. Fanti²,
 A.A. Faust³⁰, F. Fiedler²⁷, M. Fierro², H.M. Fischer³, I. Fleck⁸, R. Folman²⁶, D.G. Fong¹⁷,
 M. Foucher¹⁷, A. Fürtjes⁸, D.I. Futyan¹⁶, P. Gagnon⁷, J.W. Gary⁴, J. Gascon¹⁸,
 S.M. Gascon-Shotkin¹⁷, N.I. Geddes²⁰, C. Geich-Gimbel³, T. Geralis²⁰, G. Giacomelli²,
 P. Giacomelli⁴, R. Giacomelli², V. Gibson⁵, W.R. Gibson¹³, D.M. Gingrich^{30,a}, D. Glenzinski⁹,
 J. Goldberg²², M.J. Goodrick⁵, W. Gorn⁴, C. Grandi², E. Gross²⁶, J. Grunhaus²³, M. Gruwé⁸,
 C. Hajdu³², G.G. Hanson¹², M. Hansroul⁸, M. Hapke¹³, C.K. Hargrove⁷, P.A. Hart⁹,
 C. Hartmann³, M. Hauschild⁸, C.M. Hawkes⁵, R. Hawkings²⁷, R.J. Hemingway⁶, M. Herndon¹⁷,
 G. Herten¹⁰, R.D. Heuer⁸, M.D. Hildreth⁸, J.C. Hill⁵, S.J. Hillier¹, P.R. Hobson²⁵, R.J. Homer¹,
 A.K. Honma^{28,a}, D. Horváth^{32,c}, K.R. Hossain³⁰, R. Howard²⁹, P. Hütemeyer²⁷,
 D.E. Hutchcroft⁵, P. Igo-Kemenes¹¹, D.C. Imrie²⁵, M.R. Ingram¹⁶, K. Ishii²⁴, A. Jawahery¹⁷,
 P.W. Jeffreys²⁰, H. Jeremie¹⁸, M. Jimack¹, A. Joly¹⁸, C.R. Jones⁵, G. Jones¹⁶, M. Jones⁶,
 U. Jost¹¹, P. Jovanovic¹, T.R. Junk⁸, D. Karlen⁶, V. Kartvelishvili¹⁶, K. Kawagoe²⁴,
 T. Kawamoto²⁴, P.I. Kayal³⁰, R.K. Keeler²⁸, R.G. Kellogg¹⁷, B.W. Kennedy²⁰, J. Kirk²⁹,
 A. Klier²⁶, S. Kluth⁸, T. Kobayashi²⁴, M. Kobel¹⁰, D.S. Koetke⁶, T.P. Kokott³, M. Kolrep¹⁰,
 S. Komamiya²⁴, T. Kress¹¹, P. Krieger⁶, J. von Krogh¹¹, P. Kyberd¹³, G.D. Lafferty¹⁶,
 R. Lahmann¹⁷, W.P. Lai¹⁹, D. Lanske¹⁴, J. Lauber¹⁵, S.R. Lautenschlager³¹, J.G. Layter⁴,
 D. Lazic²², A.M. Lee³¹, E. Lefebvre¹⁸, D. Lellouch²⁶, J. Letts¹², L. Levinson²⁶, S.L. Lloyd¹³,
 F.K. Loebinger¹⁶, G.D. Long²⁸, M.J. Losty⁷, J. Ludwig¹⁰, A. Macchiolo², A. Macpherson³⁰,
 M. Mannelli⁸, S. Marcellini², C. Markus³, A.J. Martin¹³, J.P. Martin¹⁸, G. Martinez¹⁷,
 T. Mashimo²⁴, P. Mättig³, W.J. McDonald³⁰, J. McKenna²⁹, E.A. Mckigney¹⁵, T.J. McMahon¹,
 R.A. McPherson⁸, F. Meijers⁸, S. Menke³, F.S. Merritt⁹, H. Mes⁷, J. Meyer²⁷, A. Michelini²,
 G. Mikenberg²⁶, D.J. Miller¹⁵, A. Mincer^{22,e}, R. Mir²⁶, W. Mohr¹⁰, A. Montanari², T. Mori²⁴,
 M. Morii²⁴, U. Müller³, S. Mihara²⁴, K. Nagai²⁶, I. Nakamura²⁴, H.A. Neal⁸, B. Nellen³,
 R. Nisius⁸, S.W. O’Neale¹, F.G. Oakham⁷, F. Odorici², H.O. Ogren¹², A. Oh²⁷,
 N.J. Oldershaw¹⁶, M.J. Oreglia⁹, S. Orito²⁴, J. Pálincás^{33,d}, G. Pásztor³², J.R. Pater¹⁶,
 G.N. Patrick²⁰, J. Patt¹⁰, M.J. Pearce¹, R. Perez-Ochoa⁸, S. Petzold²⁷, P. Pfeifenschneider¹⁴,
 J.E. Pilcher⁹, J. Pinfold³⁰, D.E. Plane⁸, P. Poffenberger²⁸, B. Poli², A. Posthaus³, D.L. Rees¹,
 D. Rigby¹, S. Robertson²⁸, S.A. Robins²², N. Rodning³⁰, J.M. Roney²⁸, A. Rooke¹⁵, E. Ros⁸,
 A.M. Rossi², P. Routenburg³⁰, Y. Rozen²², K. Runge¹⁰, O. Runolfsson⁸, U. Ruppel¹⁴,
 D.R. Rust¹², R. Rylko²⁵, K. Sachs¹⁰, T. Saeki²⁴, E.K.G. Sarkisyan²³, C. Sbarra²⁹, A.D. Schaile³⁴,
 O. Schaile³⁴, F. Scharf³, P. Scharff-Hansen⁸, P. Schenk³⁴, J. Schieck¹¹, P. Schleper¹¹,
 B. Schmitt⁸, S. Schmitt¹¹, A. Schöning⁸, M. Schröder⁸, H.C. Schultz-Coulon¹⁰, M. Schumacher³,
 C. Schwick⁸, W.G. Scott²⁰, T.G. Shears¹⁶, B.C. Shen⁴, C.H. Shepherd-Themistocleous⁸,

P. Sherwood¹⁵, G.P. Siroli², A. Sittler²⁷, A. Skillman¹⁵, A. Skuja¹⁷, A.M. Smith⁸, G.A. Snow¹⁷, R. Sobie²⁸, S. Söldner-Rembold¹⁰, R.W. Springer³⁰, M. Sproston²⁰, K. Stephens¹⁶, J. Steuerer²⁷, B. Stockhausen³, K. Stoll¹⁰, D. Strom¹⁹, P. Szymanski²⁰, R. Tafirout¹⁸, S.D. Talbot¹, S. Tanaka²⁴, P. Taras¹⁸, S. Tarem²², R. Teuscher⁸, M. Thiergen¹⁰, M.A. Thomson⁸, E. von Törne³, S. Towers⁶, I. Trigger¹⁸, Z. Trócsányi³³, E. Tsur²³, A.S. Turcot⁹, M.F. Turner-Watson⁸, P. Utzat¹¹, R. Van Kooten¹², M. Verzocchi¹⁰, P. Vikas¹⁸, E.H. Vokurka¹⁶, H. Voss³, F. Wäckerle¹⁰, A. Wagner²⁷, C.P. Ward⁵, D.R. Ward⁵, P.M. Watkins¹, A.T. Watson¹, N.K. Watson¹, P.S. Wells⁸, N. Wermes³, J.S. White²⁸, B. Wilkens¹⁰, G.W. Wilson²⁷, J.A. Wilson¹, G. Wolf²⁶, T.R. Wyatt¹⁶, S. Yamashita²⁴, G. Yekutieli²⁶, V. Zacek¹⁸, D. Zer-Zion⁸

¹School of Physics and Space Research, University of Birmingham, Birmingham B15 2TT, UK

²Dipartimento di Fisica dell' Università di Bologna and INFN, I-40126 Bologna, Italy

³Physikalisches Institut, Universität Bonn, D-53115 Bonn, Germany

⁴Department of Physics, University of California, Riverside CA 92521, USA

⁵Cavendish Laboratory, Cambridge CB3 0HE, UK

⁶Ottawa-Carleton Institute for Physics, Department of Physics, Carleton University, Ottawa, Ontario K1S 5B6, Canada

⁷Centre for Research in Particle Physics, Carleton University, Ottawa, Ontario K1S 5B6, Canada

⁸CERN, European Organisation for Particle Physics, CH-1211 Geneva 23, Switzerland

⁹Enrico Fermi Institute and Department of Physics, University of Chicago, Chicago IL 60637, USA

¹⁰Fakultät für Physik, Albert Ludwigs Universität, D-79104 Freiburg, Germany

¹¹Physikalisches Institut, Universität Heidelberg, D-69120 Heidelberg, Germany

¹²Indiana University, Department of Physics, Swain Hall West 117, Bloomington IN 47405, USA

¹³Queen Mary and Westfield College, University of London, London E1 4NS, UK

¹⁴Technische Hochschule Aachen, III Physikalisches Institut, Sommerfeldstrasse 26-28, D-52056 Aachen, Germany

¹⁵University College London, London WC1E 6BT, UK

¹⁶Department of Physics, Schuster Laboratory, The University, Manchester M13 9PL, UK

¹⁷Department of Physics, University of Maryland, College Park, MD 20742, USA

¹⁸Laboratoire de Physique Nucléaire, Université de Montréal, Montréal, Quebec H3C 3J7, Canada

¹⁹University of Oregon, Department of Physics, Eugene OR 97403, USA

²⁰Rutherford Appleton Laboratory, Chilton, Didcot, Oxfordshire OX11 0QX, UK

²²Department of Physics, Technion-Israel Institute of Technology, Haifa 32000, Israel

²³Department of Physics and Astronomy, Tel Aviv University, Tel Aviv 69978, Israel

²⁴International Centre for Elementary Particle Physics and Department of Physics, University of Tokyo, Tokyo 113, and Kobe University, Kobe 657, Japan

²⁵Brunel University, Uxbridge, Middlesex UB8 3PH, UK

²⁶Particle Physics Department, Weizmann Institute of Science, Rehovot 76100, Israel

²⁷Universität Hamburg/DESY, II Institut für Experimental Physik, Notkestrasse 85, D-22607 Hamburg, Germany

²⁸University of Victoria, Department of Physics, P O Box 3055, Victoria BC V8W 3P6, Canada

²⁹University of British Columbia, Department of Physics, Vancouver BC V6T 1Z1, Canada

³⁰University of Alberta, Department of Physics, Edmonton AB T6G 2J1, Canada

³¹Duke University, Dept of Physics, Durham, NC 27708-0305, USA

³²Research Institute for Particle and Nuclear Physics, H-1525 Budapest, P O Box 49, Hungary

³³Institute of Nuclear Research, H-4001 Debrecen, P O Box 51, Hungary

³⁴Ludwigs-Maximilians-Universität München, Sektion Physik, Am Coulombwall 1, D-85748 Garching, Germany

^a and at TRIUMF, Vancouver, Canada V6T 2A3

^b and Royal Society University Research Fellow

^c and Institute of Nuclear Research, Debrecen, Hungary

^d and Department of Experimental Physics, Lajos Kossuth University, Debrecen, Hungary

^e and Department of Physics, New York University, NY 1003, USA

1 Introduction

Supersymmetric (SUSY) extensions [1] of the Standard Model predict the existence of the bosonic partners of all known fermions. The scalar top quark (\tilde{t}), which is the bosonic partner of the top quark, can be the lightest charged supersymmetric particle for the following two reasons [2]. Firstly, one-loop radiative corrections to the \tilde{t} mass through Higgsino-quark loops and Higgs-squark loops are always negative. The correction is large for a heavy top quark mass as measured by the CDF and D0 Collaborations [3]. Secondly, the supersymmetric partners of the right-handed and left-handed top quarks (\tilde{t}_R and \tilde{t}_L) mix, and the resultant two mass eigenstates (\tilde{t}_1 and \tilde{t}_2) have a mass splitting. This mass splitting is expected to be very large due to the large top quark mass. It is possible that the lighter mass eigenstate (\tilde{t}_1) can be lighter than any other charged SUSY particle, and also lighter than the top quark itself. The \tilde{t}_1 is the mixed state of \tilde{t}_R and \tilde{t}_L , *i.e.* $\tilde{t}_1 = \tilde{t}_L \cos \theta_{\tilde{t}} + \tilde{t}_R \sin \theta_{\tilde{t}}$, where $\theta_{\tilde{t}}$ is a mixing angle. All SUSY breaking parameters [1] are hidden in the $\theta_{\tilde{t}}$ and a mass of \tilde{t}_1 .

The scalar bottom quark (\tilde{b}) can also be light if $\tan \beta$, the ratio of vacuum expectation values of the two Higgs doublets, is larger than approximately 40. In this case, analogous mixing between the supersymmetric partners of the right- and left-handed states of the bottom quark (\tilde{b}_R and \tilde{b}_L) becomes large, and the resultant two mass eigenstates (\tilde{b}_1 and \tilde{b}_2) also have a large mass splitting [4]. The mass of the lighter mass eigenstate (\tilde{b}_1) may therefore be within the reach of LEP2.

Scalar top quark pairs and scalar bottom quark pairs are produced in e^+e^- annihilation via a virtual Z^0 boson or a virtual photon. In this paper it is assumed that R-parity [5] is conserved and that either $\tilde{\chi}_1^0$ or $\tilde{\nu}$ is the only SUSY particle which is lighter than \tilde{t}_1 (\tilde{b}_1), where $\tilde{\chi}_1^0$ is the lightest neutralino and $\tilde{\nu}$ is the scalar neutrino. The dominant decay mode of the \tilde{t}_1 with the above assumptions is expected to be either¹ $\tilde{t}_1 \rightarrow c\tilde{\chi}_1^0$ or $\tilde{t}_1 \rightarrow b\tilde{\nu}\ell^+$. Both of these decay modes have been searched for. The dominant decay mode of the \tilde{b}_1 is expected to be $\tilde{b}_1 \rightarrow b\tilde{\chi}_1^0$. Under the assumption of R-parity conservation, the $\tilde{\chi}_1^0$ and $\tilde{\nu}$ are invisible in the detector. Thus, $\tilde{t}_1\tilde{\bar{t}}_1$ and $\tilde{b}_1\tilde{\bar{b}}_1$ events are characterised by two acoplanar jets² or two acoplanar jets plus two leptons, with missing energy.

¹Through out this paper, all references to particle or decay implicitly include charge conjugation.

²Two jets not back-to-back with each other in the plane perpendicular to the beam axis.

The D0 Collaboration has reported a lower limit [6] on the \tilde{t}_1 mass of about 85 GeV (95% C.L.) for the case of $\tilde{t}_1 \rightarrow c\tilde{\chi}_1^0$ and that the mass difference between \tilde{t}_1 and $\tilde{\chi}_1^0$ is larger than about 35 GeV. Searches at e^+e^- colliders are sensitive to a smaller mass difference and mass limits for the \tilde{t}_1 have been obtained around the Z^0 peak (LEP1) assuming $\tilde{t}_1 \rightarrow c\tilde{\chi}_1^0$. A 95% C.L. lower limit of about 45 GeV was obtained for a mass difference larger than 5 GeV [7]. Previous searches at centre-of-mass energies of $\sqrt{s}=130, 136$ [8], 161 [9] and 171 GeV [10, 11] improved the limit on the mass of the \tilde{t}_1 to 66.8 GeV if the $\theta_{\tilde{t}}$ is smaller than $\pi/4$ and if the mass difference between \tilde{t}_1 and $\tilde{\chi}_1^0$ is larger than 10 GeV.

In 1997 the LEP e^+e^- collider at CERN was run at centre-of-mass energies of 181–184 GeV. The luminosity weighted mean centre-of-mass energy was 182.7 GeV. In this paper direct searches for \tilde{t}_1 and \tilde{b}_1 using the data collected with the OPAL detector at these centre-of-mass energies are reported. The results shown here have been obtained by combining the results obtained at these new centre-of-mass energies with those obtained at $\sqrt{s}=130, 136, 161$ and 171 GeV [9, 10].

The phenomenology of the production and decay of the \tilde{t}_1 (\tilde{b}_1) is described in section 2 of the previous publication [10]. In this paper, the OPAL detector and the event simulation for signal and background processes are given in section 2. In section 3, the data analysis is described and the results are given in section 4.

2 The OPAL Detector and Event Simulation

2.1 The OPAL Detector

The OPAL detector, which is described in detail in ref. [12], is a multipurpose apparatus having nearly complete solid angle coverage. The central detector consists of a silicon strip detector and tracking chambers, providing charged particle tracking for over 96% of the full solid angle, inside a uniform solenoidal magnetic field of 0.435 T. A lead-glass electromagnetic (EM) calorimeter located outside the magnet coil is hermetic in the polar angle³ range of $|\cos\theta| < 0.82$ for the barrel region and $0.81 < |\cos\theta| < 0.984$ for the endcap region. The magnet return yoke consisting of barrel and endcap sections along with pole tips is instrumented for hadron calorimetry (HCAL) in the region $|\cos\theta| < 0.99$. Four layers of muon chambers cover the outside of the hadron calorimeter. Calorimeters close to the beam axis measure the luminosity using small angle Bhabha scattering events and complete the geometrical acceptance down to 24 mrad. These include the forward detectors (FD) which are lead-scintillator sandwich calorimeters and, at smaller angles, silicon tungsten calorimeters (SW) [13] located on both sides of the interaction point. Tungsten shields were installed around the beam pipe in front of the SW detectors to reduce the amount of synchrotron radiation seen by the detector. The presence of the shield results in a gap in the SW acceptance between the polar angles of 28 and 31 mrad. The gap between the endcap EM calorimeter and the FD is filled by an additional lead-scintillator electromagnetic calorimeter, called the gamma-catcher.

³A right-handed coordinate system is adopted, where the x -axis points to the centre of the LEP ring, and positive z is along the electron beam direction. The angles θ and ϕ are the polar and azimuthal angles, respectively.

2.2 Monte Carlo Event Simulation of \tilde{t}_1 and \tilde{b}_1

Monte Carlo simulation of the production and decay of the \tilde{t}_1 was performed as follows [14]. The $\tilde{t}_1\tilde{t}_1^*$ pairs were generated taking into account initial-state radiation [15]. The hadronisation process was subsequently performed to produce colourless \tilde{t}_1 -hadrons and other fragmentation products according to the Lund string fragmentation scheme (JETSET 7.4) [15, 16]. The parameters for perturbative QCD and fragmentation processes were optimised using event shape distributions of the hadronic Z^0 decays measured by OPAL [17]. For the fragmentation of the \tilde{t}_1 , the fragmentation function proposed by Peterson *et al.* [15, 18] was used, where the parameter $\epsilon_{\tilde{t}_1}$ was set to

$$\epsilon_{\tilde{t}_1} = \epsilon_b m_b^2 / m_{\tilde{t}_1}^2 \quad (\epsilon_b = 0.0038 [17], m_b = 5 \text{ GeV}) . \quad (1)$$

The \tilde{t}_1 -hadron was formed from a \tilde{t}_1 -quark and a spectator anti-quark or diquark [19]. The fragmentation products excluding the \tilde{t}_1 -hadrons carry less than 2% of the centre-of-mass energy. For the \tilde{t}_1 decaying into $c\tilde{\chi}_1^0$, a colour string was stretched between the charm quark and the spectator. This colour singlet system was hadronised using the Lund scheme [15, 16]. Gluon bremsstrahlung (QCD parton showering) was allowed in this process, and the Peterson function was also used for the charm quark fragmentation, where ϵ_c was set to 0.031 [17]. The signals for the decays $\tilde{t}_1 \rightarrow b\ell^+\tilde{\nu}$ and $\tilde{b}_1 \rightarrow b\tilde{\chi}_1^0$ were simulated in a similar manner.

One thousand events were generated at each of 56 combinations of $(m_{\tilde{t}_1}, m_{\tilde{\chi}_1^0})$ for $\tilde{t}_1 \rightarrow c\tilde{\chi}_1^0$, 40 combinations of $(m_{\tilde{t}_1}, m_{\tilde{\nu}})$ for $\tilde{t}_1 \rightarrow b\ell^+\tilde{\nu}$ and 40 combinations of $(m_{\tilde{t}_1}, m_{\tilde{\nu}})$ for $\tilde{t}_1 \rightarrow b\tau^+\tilde{\nu}$. The $\tilde{b}_1\tilde{b}_1^*$ events were generated for 48 combinations of $(m_{\tilde{b}_1}, m_{\tilde{\chi}_1^0})$. The mixing angles of the \tilde{t}_1 and \tilde{b}_1 were set to zero when these events were generated. The dependence of the detection efficiencies on these mixing angles will be discussed in section 4.1. The generated events were processed through the full simulation of the OPAL detector [20], and the same event analysis chain was applied to the simulated events and the data.

2.3 Monte Carlo Event Simulation of Background Processes

The background processes were simulated as follows:

- Multijet hadronic events $e^+e^- \rightarrow q\bar{q}(\gamma)$ in which one or two jet momenta are mismeasured are a background for the large Δm region ($\equiv m_{\tilde{t}_1} - m_{\tilde{\chi}_1^0}, m_{\tilde{t}_1} - m_{\tilde{\nu}}, \text{ or } m_{\tilde{b}_1} - m_{\tilde{\chi}_1^0}$). The PYTHIA [15] generator was used to simulate hadronic events.
- τ pairs, in which one of the τ lepton decays into a low momentum electron and energetic neutrinos, are a background to acoplanar two-jet events. The KORALZ event generator [21] was used for the generation of $\tau^+\tau^-(\gamma)$ and $\mu^+\mu^-(\gamma)$ events. The BHWIDE program [22] was used for $e^+e^- \rightarrow e^+e^-(\gamma)$ events.
- Two-photon processes are the most important background for the case of a small mass difference Δm , since such signal events have small visible energy and small transverse momentum relative to the beam direction. Using the Monte Carlo generators PHOJET [23], PYTHIA [15] and HERWIG [24], hadronic events from two-photon processes were simulated in which the invariant mass of the photon-photon system ($M_{\gamma\gamma}$) was larger than 5.0 GeV. Monte Carlo samples for four-lepton events ($e^+e^-e^+e^-$, $e^+e^-\mu^+\mu^-$ and $e^+e^-\tau^+\tau^-$) were generated with the Vermaseren program [25].

- Finally, four-fermion processes in which at least one of the fermions is a neutrino constitute a serious background. The dominant contributions come from W^+W^- or γ^*Z^0 events. Since the interference effects of various diagrams are important, the grc4f generator [26] was used, which takes into account all interfering diagrams and includes initial-state photon radiation.

These background events were also processed through the full detector simulation and the same event analysis chain as used for the data was applied.

3 Analysis

The present analysis is based on the data collected during the 1997 run of LEP2. Since the event topologies of $\tilde{t}_1 \rightarrow c\tilde{\chi}_1^0$ and $\tilde{b}_1 \rightarrow b\tilde{\chi}_1^0$ are similar, the same selection criteria were used for both these modes (section 3.1 analysis A). In section 3.2 (analysis B), the selection criteria for $\tilde{t}_1 \rightarrow b\ell^+\tilde{\nu}$ are discussed. These analyses are similar to those in ref. [10], and the same quality criteria as in ref. [10] were used to select tracks and clusters.

Variables used for the cuts, such as the total visible energy, E_{vis} , the total transverse momentum and the acoplanarity angle (defined below) were calculated as follows. First, the four-momenta of the tracks and those of the EM and HCAL clusters not associated with charged tracks were summed. Whenever a calorimeter cluster had associated charged tracks, the expected energy deposited by the tracks was subtracted from the cluster energy to reduce double counting. If the energy of a cluster was smaller than the expected energy deposited by the associated tracks, the cluster energy was not used. Hadron calorimeter clusters were also used in calculating event variables. A large momentum-unbalance is occasionally caused by the fluctuation in the energy measurement of clusters in the hadron calorimeter because of the limited energy resolution. Therefore the transverse momentum and the visible mass calculated without the HCAL clusters were also used to reduce two-photon background processes.

The following preselection criteria (P1 – P2), which are common to both analyses A and B, were applied first. The numbers of events remaining after each cut are listed in Table 1. For comparison, the table also shows the corresponding numbers of simulated events for background processes and for three samples of the simulated $\tilde{t}_1\tilde{\bar{t}}_1$ ($\tilde{t}_1 \rightarrow c\tilde{\chi}_1^0$) and $\tilde{b}_1\tilde{\bar{b}}_1$ events.

(P1) The number of charged tracks was required to be at least four. The ratio of the number of good tracks to the total number of reconstructed tracks was required to be greater than 0.2 to reduce beam-gas and beam-wall background events. The visible mass of the event, excluding the hadron calorimeter, was also required to be larger than 3 GeV.

(P2) To reduce the background from two-photon processes and multihadronic events, where a jet axis was close to the beam direction, the total energy deposited had to be less than 5 GeV in each SW detector, less than 2 GeV in each FD detector and less than 5 GeV in each side of the gamma-catcher.

3.1 Analysis A: $\tilde{t}_1 \rightarrow c\tilde{\chi}_1^0$ and $\tilde{b}_1 \rightarrow b\tilde{\chi}_1^0$

The experimental signature for $\tilde{t}_1\tilde{\bar{t}}_1$ ($\tilde{t}_1 \rightarrow c\tilde{\chi}_1^0$) events and $\tilde{b}_1\tilde{\bar{b}}_1$ events is an acoplanar two-jet topology with a large transverse momentum with respect to the beam axis. The fragmentation

functions of \tilde{t}_1 and \tilde{b}_1 are very hard and the invariant mass of charm (bottom) quark and the spectator quark is small, therefore the jets are expected to be narrow.

The event selection criteria are described below. The numbers of events remaining after each cut are also listed in Table 1.

- (A1) The visible energy in the region of $|\cos\theta| > 0.9$ was required to be less than 20% of the total visible energy. In addition, the polar angle of the missing momentum direction, θ_{miss} , was required to satisfy $|\cos\theta_{\text{miss}}| < 0.9$ to reduce the two-photon and beam-gas events.
- (A2) Events from two-photon processes were largely removed by demanding that the event transverse momentum excluding the hadron calorimeter, P_t , be greater than 4.5 GeV and that the transverse momentum including the hadron calorimeter, P_t^{HCAL} , be greater than 4.5 GeV. Fig. 1 shows the distribution of P_t just before these cuts.
- (A3) The number of reconstructed jets was required to be exactly two. Jets were reconstructed using the Durham algorithm [27] with the jet resolution parameter of $y_{\text{cut}} = 0.005(E_{\text{vis}}/\sqrt{s})^{-1}$. This E_{vis} -dependent y_{cut} parameter was necessary for good jet-reconstruction over a wide range of $m_{\tilde{t}_1}$, $m_{\tilde{b}_1}$ and $m_{\tilde{\chi}_1^0}$. Fig. 2 shows the number of reconstructed jets before this cut. Furthermore, both reconstructed jets were required to contain at least two charged particles to reduce the $\tau^+\tau^-$ background where at least one of the τ 's decayed into only one charged particle.
- (A4) The acoplanarity angle, ϕ_{acop} , is defined as π minus the azimuthal opening angle between the directions of the two reconstructed jets. To ensure the reliability of the calculation of ϕ_{acop} , both jet axes were required to satisfy $|\cos\theta_{\text{jet}}| < 0.95$, where θ_{jet} is the polar angle of the jet. The value of ϕ_{acop} was required to be greater than 20° . Fig. 3 shows the distributions of ϕ_{acop} just before this selection.
- (A5) ‘Softness’ was defined as $(\frac{M_1}{E_1} + \frac{M_2}{E_2})$, where M_1 and M_2 are the invariant masses of the two reconstructed jets, and E_1 and E_2 are the energies of the jets. The signal events have low values of ‘Softness’, on the other hand, the two-photon events, which pass through the acoplanarity cut, have relatively large values. It was required that $1.5 \times \text{Softness} < (P_t - 4.5)$, where P_t is given in units of GeV. Fig. 4 shows the scatter plots of Softness versus P_t for data, the simulated two-photon events, the $\tilde{t}_1\bar{\tilde{t}}_1$ and $\tilde{b}_1\bar{\tilde{b}}_1$ events.
- (A6) The arithmetic mean of the invariant masses of the jets, \bar{M}_{jet} , was required to be smaller than 8 GeV. When the invariant mass of the event, M_{vis} , was larger than 65 GeV, a harder cut $\bar{M}_{\text{jet}} < 5$ GeV was applied to reduce background from $W\nu$ events. Fig. 5 shows the scatter plots of M_{vis} versus \bar{M}_{jet} for data, the simulated four-fermion events, the $\tilde{t}_1\bar{\tilde{t}}_1$ and $\tilde{b}_1\bar{\tilde{b}}_1$ events. As shown in Fig. 5(c) and (d), jets from the \tilde{t}_1 and \tilde{b}_1 are expected to have low invariant masses, because the fragmentation function of the \tilde{t}_1 is hard and only a few particles are emitted from the fragmentation process of $\tilde{t}_1\bar{\tilde{t}}_1$.

After all the cuts, no events were observed in the data, which is consistent with the expected number of background events of 2.0. The four-fermion processes are the dominant background processes. Uncertainties in the number of background for these processes will be discussed in Section 4.2.

	data	total bkg.	$q\bar{q}(\gamma)$	$\ell^+\ell^-(\gamma)$	$\gamma\gamma$	4-f	$\tilde{t}_1\bar{\tilde{t}}_1$ and $\tilde{b}_1\bar{\tilde{b}}_1$		
$m_{\tilde{t}_1}$ (GeV)							80	80	–
$m_{\tilde{b}_1}$ (GeV)							–	–	80
$m_{\tilde{\chi}_1^0}$ (GeV)							75	60	60
Presel. 1	275501	250435	5028	1229	243137	1042	874	967	994
Presel. 2	141619	124394	3618	1165	118753	859	848	933	960
cut (A1)	22927	19583	1126	236	17651	569	731	768	809
cut (A2)	1441	1461	771	156	47.1	488	458	745	778
cut (A3)	362	359	298	10.4	16.3	34.0	305	649	717
cut (A4)	15	25.3	0.09	0.06	3.41	21.8	289	582	638
cut (A5)	15	22.3	0.08	0.06	0.38	21.7	229	582	636
cut (A6)	0	1.97	0.04	0.04	0.27	1.63	229	576	609

Table 1: The remaining numbers of events normalised to the integrated luminosity of the data for various background processes are compared with data after each cut. Numbers for three simulated event samples of $\tilde{t}_1\bar{\tilde{t}}_1$ and $\tilde{b}_1\bar{\tilde{b}}_1$ are also given (each starting from 1000 events). Before the cut (A2) was applied, there is a discrepancy between data and the simulated background processes, since the numbers of events expected from two-photon processes do not include the region $M_{\gamma\gamma} < 5$ GeV.

The efficiencies for $\tilde{t}_1\bar{\tilde{t}}_1$ and $\tilde{b}_1\bar{\tilde{b}}_1$ events are listed in Tables 2 and 3. Both efficiencies are 30–60%, if the mass difference between the $\tilde{t}_1(\tilde{b}_1)$ and $\tilde{\chi}_1^0$ is larger than 10 GeV. A modest efficiency of about 20% is also obtained for a mass difference of 5 GeV for $\tilde{t}_1\bar{\tilde{t}}_1$ events. In addition to effects included in the detector simulation, an additional efficiency loss of 3.6% (relative) arose from beam-related background in the SW, FD and gamma-catcher detectors estimated using random beam crossing events. The efficiencies given in Tables 1–5 do not include this correction, but it is included when deriving the mass limits. The efficiency at an arbitrary point was estimated using a polynomial fit to the efficiencies determined using the Monte Carlo simulations.

3.2 Analysis B: $\tilde{t}_1 \rightarrow b\ell\tilde{\nu}$

The experimental signature for $\tilde{t}_1\bar{\tilde{t}}_1(\tilde{t}_1 \rightarrow b\ell\tilde{\nu})$ events is an two acoplanar jets plus two leptons with missing transverse momentum with respect to the beam axis. The momenta of leptons and the missing transverse momentum depend strongly on the mass difference between \tilde{t}_1 and $\tilde{\nu}$. To obtain optimal performance, two sets of selection criteria (analyses B-L and B-H) were applied depending on this mass difference. If the mass difference is smaller than or equal to 10 GeV, the momenta of leptons and the missing transverse momentum are relatively small. In such cases, it is difficult to identify leptons effectively and the dominant background comes from two-photon processes. Selections were optimised to reduce these two-photon events. When the mass difference is larger than 10 GeV, the momenta of leptons and the missing transverse momentum become large. In such cases the four-fermion processes become the dominant background processes.

The numbers of events remaining after each cut are listed in Tables 4 and 5. For comparison,

$m_{\tilde{t}_1}$ (GeV)	50	55	60	65	70	75	80	85
Δm								
3 GeV	11	9	7	6	5	3	2	2
5 GeV	29	30	27	28	27	25	23	22
10 GeV	40	44	45	48	49	48	48	49
20 GeV	36	45	49	52	53	58	58	60
$m_{\tilde{t}_1}/2$	35	38	41	45	44	47	51	52
$m_{\tilde{t}_1} - 10$ GeV	27	28	28	29	32	35	40	40
$m_{\tilde{t}_1}$	24	27	29	29	33	33	37	36

Table 2: The detection efficiencies in percent for $\tilde{t}_1\bar{\tilde{t}}_1$, in which \tilde{t}_1 decays into $c\tilde{\chi}_1^0$ for different \tilde{t}_1 masses and Δm values, where Δm is $m_{\tilde{t}_1} - m_{\tilde{\chi}_1^0}$. The statistical fluctuations of these efficiencies are about 2% (absolute).

$m_{\tilde{b}_1}$ (GeV)	50	55	60	65	70	75	80	85
Δm								
7 GeV	34	34	36	36	35	38	37	36
10 GeV	40	43	46	46	50	49	50	49
20 GeV	36	41	48	51	55	59	61	63
$m_{\tilde{b}_1}/2$	29	34	35	37	37	41	47	50
$m_{\tilde{b}_1} - 10$ GeV	22	22	22	25	25	27	32	33
$m_{\tilde{b}_1}$	21	23	21	22	23	26	31	31

Table 3: The detection efficiencies in percent for $\tilde{b}_1\bar{\tilde{b}}_1$ for different \tilde{b}_1 masses and Δm values, where $\Delta m = m_{\tilde{b}_1} - m_{\tilde{\chi}_1^0}$. The statistical fluctuations of these efficiencies are about 2% (absolute).

the table also shows the corresponding numbers for simulated events for background processes and for two samples of simulated $\tilde{t}_1\bar{\tilde{t}}_1$ events, in which the branching fraction to each lepton flavour is assumed to be the same.

3.2.1 Small mass difference case

For the case of small mass difference ($\Delta m \leq 10$ GeV), the following selections were applied.

- (B-L1) The visible energy in the region of $|\cos\theta| > 0.9$ was required to be less than 10% of the total visible energy. In addition, $|\cos\theta_{\text{miss}}| < 0.8$ was required.
- (B-L2) Both P_t and P_t^{HCAL} were required to be greater than 5 GeV.
- (B-L3) The number of charged tracks was required to be at least six. Furthermore, the number of reconstructed jets was required to be at least four, because the signal should contain two hadronic jets plus two isolated leptons. Jets were reconstructed using the Durham algorithm [27] with the jet resolution parameter of $y_{\text{cut}} = 0.004$. Fig. 6 shows the distributions of the number of reconstructed jets before this selection.
- (B-L4) To examine the acoplanarity of the events, jets were reconstructed using the Durham algorithm where the number of jets was forced to be two. To ensure a good measurement

of acoplanarity angle, $|\cos \theta_{\text{jet}}| < 0.95$ was required for both reconstructed jets. Finally, the acoplanarity angle between these two jets was required to be greater than 15° . In the three-body decay, the transverse momentum carried by the $\tilde{\nu}$ with respect to the original \tilde{t}_1 -momentum is smaller than that of $\tilde{\chi}_1^0$ in the two-body decay. When the \tilde{t}_1 is light, the outgoing $\tilde{\nu}$ is strongly boosted toward the direction of the parent \tilde{t}_1 . Hence ϕ_{acop} for the signal becomes small. This is the reason for the use of a looser acoplanarity angle cut.

(B-L5) The total visible energy normalised to the centre-of-mass energy, E_{vis}/\sqrt{s} , was required to be smaller than 0.2 to reject four-fermion events.

No events were observed in the data after the above cuts. The number of expected background events is 1.1. Two-photon processes are the dominant background. Uncertainties in the number of expected background events will be discussed in Section 4.2.

	data	total bkg.	$q\bar{q}(\gamma)$	$\ell^+\ell^-(\gamma)$	$\gamma\gamma'$	4-f	$\tilde{t}_1\tilde{\bar{t}}_1$	
$m_{\tilde{t}_1}$ (GeV)							80	80
$m_{\tilde{\nu}}$ (GeV)							73	70
cut (B-L1)	11713	9354	904	134	7859	457	717	695
cut (B-L2)	1064	1076	592	78.3	18.2	388	139	440
cut (B-L3)	287	295	94.8	0.02	1.84	198	137	435
cut (B-L4)	60	62.6	3.33	0.00	0.97	58.3	118	379
cut (B-L5)	0	1.07	0.01	0.00	0.97	0.09	118	378

Table 4: The remaining numbers of events normalised to the integrated luminosity of the data for various background processes are compared with data after each cut. Numbers for two simulated event samples of $\tilde{t}_1\tilde{\bar{t}}_1$ are also given (each starting from 1000 events). In these samples, the branching fraction to each lepton flavour is assumed to be the same. Before the cut (B-L2), there is a discrepancy between data and the simulated background processes, since the numbers of events expected from two-photon processes do not include the region $M_{\gamma\gamma} < 5$ GeV.

3.2.2 Large mass difference case

The selections for a large mass difference ($\Delta m > 10$ GeV), are described below. Because the momenta of the leptons for this case are high enough to be identified, it was required that events contained at least one lepton. Then the other cuts (B-H1 and B-H3) were relaxed compared to the small mass difference case.

(B-H1) Cut (A1) was applied to reduce two-photon and beam-gas events.

(B-H2) Cut (B-L2) was applied to reject two-photon events.

(B-H3) The number of charged tracks was required to be at least six, and the number of reconstructed jets was required to be at least three. Jets were reconstructed with the jet resolution parameter of $y_{\text{cut}} = 0.004$.

(B-H4) Cut (B-L4) was applied to reject multihadronic events.

- (B-H5)** A candidate event was required to contain at least one lepton. Leptons were identified in the following way: electrons were selected if they satisfied either of the two identification methods described in Ref. [28], and muons were identified using the two methods described in ref. [29]. The track momentum of the electron or muon candidate was required to be larger than 2 GeV. A jet reconstructed in cut (B-H3) was identified as a tau decay if it contained only one or three charged tracks, the invariant mass of the charged particles in the jet was smaller than 1.5 GeV, the invariant mass including energies deposited in the calorimeters was smaller than 2 GeV and the scalar sum of momenta of the charged tracks was larger than 2 GeV.
- (B-H6)** The invariant mass excluding the most energetic lepton was required to be smaller than 60 GeV in order to reject $W^+W^- \rightarrow \nu\ell q\bar{q}'$ events. As shown in Fig. 7, a large fraction of four-fermion events was rejected using this requirement.
- (B-H7)** The visible mass of the events, M_{vis} , must be smaller than 80 GeV to reduce W^+W^- background events in which one of W^\pm 's decayed into $\tau\nu$ and the other into $q\bar{q}'$ (g). If one jet from $q\bar{q}'$ (g) was misidentified as tau lepton, this event could pass through the previous cut (B-H6). Such events were rejected by this requirement. Fig. 8 shows the distribution of M_{vis} .

No events were observed in the data after the above cuts. The number of expected background events was 2.1. Uncertainties of the expected background events will be discussed in section 4.2. The detection efficiencies for $\tilde{t}_1\tilde{t}_1$ events are listed in Table 6. The efficiencies of both selection criteria (B-L and B-H) are presented in this table. As shown in this table, the detection efficiencies for $\tilde{t}_1 \rightarrow b\tau^+\tilde{\nu}_\tau$ are slightly smaller than the case in which the branching fraction to each lepton flavour is assumed to be the same.

	data	total bkg.	$q\bar{q}(\gamma)$	$\ell^+\ell^-(\gamma)$	$\gamma\gamma$	4-f	$\tilde{t}_1\tilde{t}_1$		
$m_{\tilde{t}_1}$ (GeV)							80	80	80
$m_{\tilde{\nu}}$ (GeV)							70	60	40
cut (B-H1)	22927	19603	1127	236	17670	567	856	792	784
cut (B-H2)	1360	1381	724	151	32.2	474	490	748	776
cut (B-H3)	857	915	466	1.48	8.66	438	490	743	764
cut (B-H4)	209	213	15.3	0.36	2.60	195	424	665	660
cut (B-H5)	162	162	6.59	0.33	0.32	155	369	639	637
cut (B-H6)	4	6.35	0.17	0.14	0.22	5.83	369	639	606
cut (B-H7)	0	2.05	0.15	0.06	0.22	1.62	369	639	581

Table 5: The remaining numbers of events normalised to the integrated luminosity of the data for various background processes are compared with data after each cut. Numbers for three simulated event samples of $\tilde{t}_1\tilde{t}_1$ are also given (each starting from 1000 events). In these samples, the branching fraction to each lepton flavour is assumed to be the same. Before the cut (B-H2), there is a discrepancy between data and the simulated background processes, since the numbers of events expected from two-photon processes do not include the region $M_{\gamma\gamma} < 5$ GeV.

$\tilde{t}_1 \rightarrow b\ell\tilde{\nu}$ the equal branching fractions for $\ell = e, \mu, \tau$								
$m_{\tilde{t}_1}$ (GeV)	50	55	60	65	70	75	80	85
Δm (B-L)								
7 GeV	9	11	12	12	12	12	12	9
10 GeV	16	22	30	32	35	39	38	37
Δm (B-H)								
10 GeV	30	33	36	37	36	40	37	35
20 GeV	45	52	56	60	61	63	64	65
$m_{\tilde{t}_1}/2$	41	46	48	52	50	51	58	60
$m_{\tilde{t}_1}-10$ GeV	25	26	27	27	29	26	28	27

$\tilde{t}_1 \rightarrow b\tau\tilde{\nu}_\tau$, 100% branching fraction								
$m_{\tilde{t}_1}$ (GeV)	50	55	60	65	70	75	80	85
Δm (B-L)								
7 GeV	6	6	8	8	7	6	6	4
10 GeV	16	22	26	29	31	32	29	28
Δm (B-H)								
10 GeV	19	20	21	21	22	23	22	19
20 GeV	36	40	42	46	49	50	51	52
$m_{\tilde{t}_1}/2$	35	38	44	44	48	50	54	51
$m_{\tilde{t}_1}-10$ GeV	26	29	31	29	33	32	32	35

Table 6: The detection efficiencies in percent for $\tilde{t}_1\tilde{\bar{t}}_1$, in which \tilde{t}_1 decays into $b\ell\tilde{\nu}$ ($\ell = e, \mu, \tau$). The upper half of the table shows the case in which the branching fraction to each lepton flavour is the same and the lower half shows the worst case in which the branching fraction of $\tilde{t}_1 \rightarrow b\tau\tilde{\nu}_\tau$ is 100%. In both tables, Δm is defined as $m_{\tilde{t}_1} - m_{\tilde{\nu}}$. The efficiencies in the first two lines of each table were obtained using the analysis B-L, the the last four lines using analysis B-H.

4 Results

No evidence for $\tilde{t}_1\tilde{\bar{t}}_1$ and $\tilde{b}_1\tilde{\bar{b}}_1$ pair-production has been observed in the data. The data are consistent with the expected background of 1.9 events in analysis A, and 1.0 and 2.0 events⁴ in analysis B for an integrated luminosity of 56.8 pb⁻¹. The sum of the expected number of background is 4.5 events subtracting overlap between three analyses. Uncertainties of expected background will be discussed in section 4.2.

4.1 Systematic Errors in the number of expected signal events

The following sources of systematic error on the expected number of the signal events were taken into account:

⁴These numbers were corrected for the inefficiency due to beam-related background events.

1. The statistical error of the signal Monte Carlo simulation is 2–10% depending on detection efficiencies.

2. The dependence of the detection efficiency on the mixing angle:

The energy distribution of the initial-state radiation depends on the mixing angle of the \tilde{t}_1 (\tilde{b}_1), because it influences the coupling between the \tilde{t}_1 (\tilde{b}_1) and the Z^0 . When the coupling is large, the initial-state radiation is hard. The detection efficiencies therefore depend on $\theta_{\tilde{t}}$ ($\theta_{\tilde{b}}$). However, the detection efficiencies in Tables 2, 3 and 6 were calculated using the simulated events which were generated for $\theta_{\tilde{t}} = \theta_{\tilde{b}} = 0.0$.

The detection efficiencies in the two extreme cases of \tilde{t}_1 decoupled from the Z^0 ($\theta_{\tilde{t}} = 0.98$) and $\tilde{t}_1 = \tilde{t}_L$ ($\theta_{\tilde{t}} = 0.0$) were compared for various $m_{\tilde{t}_1}$ values. The difference was always found to be within 2%. The effect on efficiencies for $\tilde{t}_1 \rightarrow b\ell\tilde{\nu}$ and $\tilde{b}_1 \rightarrow b\tilde{\chi}_1^0$ was also checked and similar results were obtained. The systematic error due to the dependence on the mixing angle was taken to be 2%.

3. Fragmentation function for \tilde{t}_1 :

The fragmentation scheme proposed by Peterson *et al.* was used, with the fragmentation parameter $\epsilon_{\tilde{t}_1}$ determined by equation (1). The error on $\epsilon_{\tilde{t}_1}$ was propagated from $\delta\epsilon_b/\epsilon_b = \pm 0.26$ [17] and $\delta m_b/m_b = \pm 0.06$ [30], corresponding to $\delta\epsilon_{\tilde{t}_1}/\epsilon_{\tilde{t}_1} = \pm 0.27$. The systematic error in the efficiencies due to this uncertainty was evaluated by altering the $\epsilon_{\tilde{t}_1}$ parameter by one standard deviation for several combinations of $(m_{\tilde{t}_1}, m_{\tilde{\chi}_1^0})$ and $(m_{\tilde{t}_1}, m_{\tilde{\nu}})$. For the $\tilde{t}_1 \rightarrow c\tilde{\chi}_1^0$ mode, the detection efficiencies changed by no more than 5% over the $m_{\tilde{t}_1}$ range. The relative changes for the $\tilde{t}_1 \rightarrow b\ell\tilde{\nu}$ mode were found to be 6–10%, and they depended mainly on $m_{\tilde{t}_1}$.

To estimate the dependence on the fragmentation scheme, the fragmentation function proposed by Bowler [31] was used, because the shape of this fragmentation function is very different from that of the Peterson function. The relative difference in efficiencies between the two fragmentation models was 2–3% for the $\tilde{t}_1 \rightarrow c\tilde{\chi}_1^0$ mode, which was smaller than that due to the variation of the $\epsilon_{\tilde{t}_1}$ parameter used in the Peterson fragmentation scheme. The systematic error due to the dependence on the fragmentation model was taken to be 3%. For the $\tilde{t}_1 \rightarrow b\ell\tilde{\nu}$ mode, the relative difference in efficiencies was found to lie between 4–8%, where the range was mainly due to $m_{\tilde{t}_1}$.

4. Fragmentation function for \tilde{b}_1 :

The error due to the fragmentation function for \tilde{b}_1 was also estimated using the methods described above. The uncertainty in $\epsilon_{\tilde{b}_1}$ made a relative difference of 4–6% in the efficiencies.

5. Fragmentation of the charm and bottom quarks:

The error in the efficiencies for the $\tilde{t}_1 \rightarrow c\tilde{\chi}_1^0$ mode, due to the uncertainty in ϵ_c , was estimated to be typically 3% by changing ϵ_c by $\delta\epsilon_c/\epsilon_c = \pm 0.35$ [17].

The uncertainty in the ϵ_b parameter also contributes to the error in the efficiencies for the $\tilde{t}_1 \rightarrow b\ell\tilde{\nu}$ and $\tilde{b}_1 \rightarrow b\tilde{\chi}_1^0$ modes. As mentioned above, the ϵ_b parameter was simultaneously changed by $\pm 26\%$ when $\epsilon_{\tilde{t}_1}$ and $\epsilon_{\tilde{b}_1}$ were altered. The systematic error due to the uncertainty on ϵ_b is therefore taken into account in the errors $\delta\epsilon_{\tilde{t}_1}$ and $\delta\epsilon_{\tilde{b}_1}$.

6. Fermi motion of the spectator quark in \tilde{t}_1 (\tilde{b}_1) -hadron decay:
Due to the Fermi motion of the spectator quark the invariant mass of the hadronic decay products of a \tilde{t}_1 (\tilde{b}_1) -hadron varies. For $\tilde{t}_1 \rightarrow c\tilde{\chi}_1^0$ and $\tilde{b}_1 \rightarrow b\tilde{\chi}_1^0$ modes this effect is not negligible when Δm is large. The systematic error in the efficiencies due to the Fermi motion was evaluated by altering the mass of spectator quarks. For the case of a 80 GeV \tilde{t}_1 (\tilde{b}_1) and a massless neutralino the efficiency varies by up to 6% (8%) due to the jet mass cut (A6).
7. Lepton identification:
The systematic error on electron identification was estimated to be 4% and the error on muon identification was 2%. The systematic error on tau identification is dominated by the uncertainties in the fragmentation of the bottom quark, which has already been included in the uncertainty in the ϵ_b parameter. A conservative error of 4% was applied for all types of leptons.
8. Systematic errors due to imperfections in the Monte Carlo simulation of P_t , P_t^{HCAL} , the number of reconstructed jets, E_{vis} and M_{vis} were estimated to be 3%.
9. The integrated luminosity was calculated using the SW detector. The systematic error on this luminosity was determined to be 0.26% (stat.) and 0.41% (syst.).
10. The systematic error due to the uncertainty on the trigger efficiency was estimated to be negligible. This is expected because of the requirement of at least four good tracks.

The various systematic errors are summarised in Table 7. These systematic errors were considered to be independent and the total systematic error was calculated as the quadratic sum of the individual errors. These systematic errors were treated as in Ref. [32] in calculating the limits.

Sources	$\tilde{t}_1 \rightarrow c\tilde{\chi}_1^0$	$\tilde{t}_1 \rightarrow b\ell\tilde{\nu}$	$\tilde{b}_1 \rightarrow b\tilde{\chi}_1^0$
Statistical error of MC	2–10%		
$\theta_{\tilde{t}}$ dependence	2%	2%	–
$\theta_{\tilde{b}}$ dependence	–	–	2–4%
Uncertainty on $\epsilon_{\tilde{t}_1}$	5%	6–10%	–
Uncertainty on $\epsilon_{\tilde{b}_1}$	–	–	4–6%
Fragmentation scheme	3%	4–8%	4–10%
Uncertainty on ϵ_c	3%	–	–
Uncertainty on ϵ_b	–	Included in the uncertainties of $\epsilon_{\tilde{t}_1}$ and $\epsilon_{\tilde{b}_1}$	
Spectator Fermi motion	3–6%	4%	3–8%
Uncertainty of lepton ID	–	4%	–
Detector simulation	3%		
Luminosity	0.5%		
Trigger efficiencies	negligibly small		

Table 7: The summary of the systematic errors on the expected number of the signal events. The range of these errors depend on the mass of \tilde{t}_1 and \tilde{b}_1 .

4.2 Systematic Errors in the number of background events

The two-photon and four-fermion processes are the dominant background. Systematic errors in the expected number of these processes are discussed here. Since no event was observed in data, the expected number of background events was not subtracted to calculate limits. Then these errors were not used to calculate limits.

4.2.1 Two-photon processes

The systematic errors are mostly dominated by the Monte Carlo statistics for two-photon processes. The statistical fluctuations of the expected numbers (relative errors) are $\pm 0.23(85\%)$, $\pm 0.49(50\%)$ and $\pm 0.22(100\%)$ for analysis A, B-L and B-H, respectively.

Furthermore the uncertainty on the modelling of the two-photon processes was checked with data. In order to select two-photon events the visible energy was required to be smaller than 20% of \sqrt{s} , the charged multiplicity to be at least four, the visible invariant mass to be larger than 5 GeV and the forward detector vetoes (cut P2) were required. The P_t distributions of the selected events from data were compared with Monte Carlo. The shapes of the distributions agree with each other, but there is an uncertainty of 30% in the normalisation.

4.2.2 Four-fermion processes

Uncertainties in the generators of the four-fermion processes were estimated by comparing grc4f with the Excalibur [33] and PYTHIA [15] generators. The background events predicted by these different generators are summarised in Table 8. The differences larger than statistical fluctuations were found especially in analysis A. The difference between grc4f and Excalibur comes mainly from the region of $M_{q\bar{q}'} < 40$ GeV for $e^+e^- \rightarrow e\nu q\bar{q}'$ process. On the other hand, the difference between grc4f and PYTHIA comes from the region of $M_{q\bar{q}} > 15$ GeV for $e^+e^- \rightarrow \gamma^* Z^0 \rightarrow q\bar{q}\nu\bar{\nu}$ process. The prediction on this process by PYTHIA is about 60% of grc4f. These differences were considered as the systematic errors in the four-fermion processes; 1.63 ± 0.13 (stat.) $^{+0.52}_{-0.33}$ (sys.) for analysis A, 0.09 ± 0.03 (stat.) $^{+0.12}_{-0.06}$ (sys.) for analysis B-L and 1.62 ± 0.13 (stat.) $^{+0.23}_{-0.18}$ (sys.) for analysis B-H.

	grc4f	Excalibur	PYTHIA
analysis A	1.63 ± 0.13	2.15 ± 0.15	1.30 ± 0.10
analysis B-L	0.09 ± 0.03	0.21 ± 0.05	0.03 ± 0.01
analysis B-H	1.62 ± 0.13	1.85 ± 0.13	1.44 ± 0.13

Table 8: The expected numbers of four-fermion background processes predicted by different three generators. The errors shown in this table are the statistical fluctuations.

Events with two jets plus missing transverse momentum were checked with data to study the differences in analysis A. To select events with two jets and large P_t coming from the four-fermion processes, the cuts P1, P2 and A1 were applied, and the P_t was required to be greater than 10 GeV to reject two-photon processes completely. Furthermore $d_{23}^2 (\equiv y_{23} E_{\text{vis}}^2)$ was required to be smaller than 50 GeV² to select clear two-jet events, where y_{23} is the jet resolution parameter from 2 jets to 3 jets using the Durham algorithm. Finally, the acoplanarity

	DATA	grc4f	Excalibur	PYTHIA
$\phi_{\text{acop}} > 10^\circ$	19	17.2 ± 0.4	18.9 ± 0.4	17.7 ± 0.1
$\phi_{\text{acop}} > 100^\circ$	2	1.87 ± 0.15	3.25 ± 0.18	1.22 ± 0.09

Table 9: The remaining numbers of events in data and three different generators. The errors shown in this table are the statistical errors.

angle, ϕ_{acop} , was required to be larger than 10° or 100° . After these selections, the observed numbers in data were compared with the predictions by these three generators (Table 9).

In the region of $\phi_{\text{acop}} > 100^\circ$, large differences were observed in the predictions of these three generators. But all three predictions are consistent with the data, since the statistics of data is too small. We need data with higher statistics to study the four-fermion generators.

4.3 Mass Limits

4.3.1 Scalar top quark \tilde{t}_1

To calculate mass limits, the number of signal events passing through the event selections is determined as a function of $m_{\tilde{t}_1}$, $m_{\tilde{\chi}_1^0}$ (or $m_{\tilde{\nu}}$) and $\theta_{\tilde{t}}$.

Figs. 9(a), 10(a) and 11(a) show the 95% C.L. excluded regions in the $(\theta_{\tilde{t}}, m_{\tilde{t}_1})$ plane for the $\tilde{t}_1 \rightarrow c\tilde{\chi}_1^0$, $\tilde{t}_1 \rightarrow b\ell\tilde{\nu}$ ($\ell = e, \mu, \tau$) and $\tilde{t}_1 \rightarrow b\tau\tilde{\nu}$ decay modes, respectively. The branching fraction to each lepton flavour ℓ^+ depends on the composition of the lightest chargino [10]. As the chargino becomes Higgsino-like, the branching fraction into $b\tau^+\tilde{\nu}_\tau$ becomes large. In the limit that the chargino is the pure Wino state, the branching fraction to each lepton flavour is the same. Two extreme cases in which the branching fraction to each lepton flavour is the same, or the branching fraction into $b\tau^+\tilde{\nu}_\tau$ is 100%, were considered here. The 95% C.L. mass bounds are listed in Table 10 for various values of $\theta_{\tilde{t}}$. Assuming that the \tilde{t}_1 decays into $c\tilde{\chi}_1^0$, and that the mass difference between the \tilde{t}_1 and the $\tilde{\chi}_1^0$ is greater than 10 GeV, the \tilde{t}_1 is found to be heavier than 85.0 GeV, if $\theta_{\tilde{t}} = 0$. A lower limit of 81.3 GeV is obtained even if the \tilde{t}_1 decouples from the Z^0 boson. When the \tilde{t}_1 decays into $b\ell\tilde{\nu}$, the lower limit on $m_{\tilde{t}_1}$ is 83.6 GeV, assuming that the mass difference between \tilde{t}_1 and $\tilde{\nu}$ is greater than 10 GeV, that $\theta_{\tilde{t}} = 0$ and that the branching fraction to each lepton flavour is the same. The 95% C.L. excluded regions in the $(m_{\tilde{t}_1}, m_{\tilde{\chi}_1^0})$ and $(m_{\tilde{t}_1}, m_{\tilde{\nu}})$ planes are shown in Figs. 9(b), 10(b) and 11(b) for various values of $\theta_{\tilde{t}}$. In these figures, the limits calculated by the expected background events are superimposed to show the sensitivity of these analyses.

4.3.2 Scalar bottom quark \tilde{b}_1

To calculate mass limits, the number of signal events passing through the event selections is determined as a function of $m_{\tilde{b}_1}$, $m_{\tilde{\chi}_1^0}$ and $\theta_{\tilde{b}}$. Fig. 12(a) shows the 95% C.L. excluded regions in the $(\theta_{\tilde{b}}, m_{\tilde{b}_1})$ plane for the mass difference of $\Delta m (\equiv m_{\tilde{b}_1} - m_{\tilde{\chi}_1^0}) \geq 7$ GeV and $\Delta m \geq 10$ GeV. The numerical mass bounds are listed in Table 11 for various $\theta_{\tilde{b}}$. The lower limit on the \tilde{b}_1 -mass is 82.7 GeV, if Δm is greater than 7 GeV and $\theta_{\tilde{b}} = 0$. The 95% C.L. excluded regions in the $(m_{\tilde{b}_1}, m_{\tilde{\chi}_1^0})$ plane are shown in Fig. 12(b) for various $\theta_{\tilde{b}}$. In this figure, the limit calculated by the expected background events is also superimposed to show the sensitivity of this analysis.

Lower limit on $m_{\tilde{t}_1}$ (GeV)				
	$\tilde{t}_1 \rightarrow c\tilde{\chi}_1^0$		$\tilde{t}_1 \rightarrow b\ell\tilde{\nu}$ $\ell = e, \mu, \tau$	$\tilde{t}_1 \rightarrow b\tau\tilde{\nu}_\tau$ Br = 100%
$\theta_{\tilde{t}}$ (rad)	$\Delta m \geq 5$ GeV	$\Delta m \geq 10$ GeV	$\Delta m \geq 10$ GeV	$\Delta m \geq 10$ GeV
0.0	81.2	85.0	83.6	80.0
$\leq \frac{1}{8}\pi$	80.0	84.2	82.5	79.0
$\leq \frac{1}{4}\pi$	76.8	82.0	79.7	76.1
0.98	75.8	81.3	79.2	75.0

Table 10: The excluded $m_{\tilde{t}_1}$ region at 95% C.L. ($\Delta m = m_{\tilde{t}_1} - m_{\tilde{\chi}_1^0}$ or $m_{\tilde{t}_1} - m_{\tilde{\nu}}$).

Lower limit on $m_{\tilde{b}_1}$ (GeV) ($\tilde{b}_1 \rightarrow b\tilde{\chi}_1^0$)		
$\theta_{\tilde{b}}$ (rad)	$\Delta m \geq 7$ GeV	$\Delta m \geq 10$ GeV $m_{\tilde{\chi}_1^0} \geq 30$ GeV
0.0	82.7	84.0
$\leq \frac{1}{8}\pi$	81.0	82.6
$\leq \frac{1}{4}\pi$	71.9	76.2
1.17	54.4	63.7

Table 11: The excluded $m_{\tilde{b}_1}$ region at 95% C.L. ($\Delta m = m_{\tilde{b}_1} - m_{\tilde{\chi}_1^0}$)

5 Summary and Conclusion

A data sample collected using the OPAL detector corresponding to an integrated luminosity of 56.8 pb^{-1} at $\sqrt{s} = 183 \text{ GeV}$ has been analysed to search for pair production of the scalar top quark and the scalar bottom quark predicted by supersymmetric theories. R-parity was assumed to be conserved. No events remained after the selection cuts.

The 95% C.L. lower limits on the scalar top quark mass are 85.0 and 82.0 GeV, if the mixing angle of the scalar top quark is 0 and smaller than $\frac{\pi}{4}$, respectively. Even if the \tilde{t}_1 decouples from the Z^0 boson, a lower limit of 81.3 GeV is obtained. These limits were obtained assuming that the scalar top quark decays into a charm quark and the lightest neutralino and that the mass difference between the scalar top and the lightest neutralino is larger than 10 GeV.

Assuming a relatively light scalar neutrino ($37.1 \text{ GeV} [34, 30] \leq m_{\tilde{\nu}} \leq m_{\tilde{t}_1} - m_b$) the complementary decay mode of the scalar top quark in which it decays into a bottom quark, a charged lepton and the scalar neutrino has also been studied. If the mass difference between the scalar top quark and the scalar neutrino is greater than 10 GeV and if the mixing angle of the scalar top quark is 0, the 95% C.L. lower limit on the scalar top quark mass is 83.6 GeV. This limit is obtained assuming that the branching fraction to each lepton flavour is the same.

A mass limit on the light scalar bottom quark is found to be 82.7 GeV (95% C.L.), assuming that the mass difference between the scalar bottom quark and the lightest neutralino is greater than 7 GeV and that the mixing angle of the scalar bottom quark is zero. If the mass difference is greater than 10 GeV and the lightest neutralino is heavier than 30 GeV, a mass limit on the light scalar bottom quark is 84.0 GeV (95% C.L.).

Acknowledgements

We particularly wish to thank the SL Division for the efficient operation of the LEP accelerator at all energies and for their continuing close cooperation with our experimental group. We thank our colleagues from CEA, DAPNIA/SPP, CE-Saclay for their efforts over the years on the time-of-flight and trigger systems which we continue to use. In addition to the support staff at our own institutions we are pleased to acknowledge the
Department of Energy, USA,
National Science Foundation, USA,
Particle Physics and Astronomy Research Council, UK,
Natural Sciences and Engineering Research Council, Canada,
Israel Science Foundation, administered by the Israel Academy of Science and Humanities,
Minerva Gesellschaft,
Benozio Center for High Energy Physics,
Japanese Ministry of Education, Science and Culture (the Monbusho) and a grant under the Monbusho International Science Research Program,
German Israeli Bi-national Science Foundation (GIF),
Bundesministerium für Bildung, Wissenschaft, Forschung und Technologie, Germany,
National Research Council of Canada,
Research Corporation, USA,
Hungarian Foundation for Scientific Research, OTKA T-016660, T023793 and OTKA F-023259.

References

- [1] Y. Gol'fand and E. Likhtam, JETP Lett. **13** (1971) 323;
D. Volkov and V. Akulov, Phys. Lett. **B46** (1973) 109;
J. Wess and B. Zumino, Nucl. Phys. **B70** (1974) 39.
- [2] M. Drees and K. Hikasa, Phys. Lett. **B252** (1990) 127;
K. Hikasa and M. Kobayashi, Phys. Rev. **D36** (1987) 724;
J. Ellis and S. Rudaz, Phys. Lett. **B128** (1983) 248;
G. Altarelli and R. Rückl, Phys. Lett. **B144** (1984) 126;
S. Dawson, E. Eichten and C. Quigg, Phys. Rev. **D31** (1985) 1581;
J. Ellis, G.L. Fogli and E. Lisi, Nucl. Phys. **B393** (1993) 3.
- [3] CDF Collab., F. Abe *et al.*, Phys. Rev. Lett. **80** (1998) 2779;
D0 Collab., S. Abachi *et al.*, FERMILAB-PUB-98-031-E, submitted to Phys. Rev. D.
- [4] A. Bartl, W. Majerotto and W. Porod, Z. Phys, **C64** (1994) 499.
- [5] P. Fayet, Phys. Lett. **B69** (1977) 489.
- [6] D0 Collab., F. Abachi *et al.*, Phys. Rev. Lett. **76** (1996) 2222.
- [7] OPAL Collab., R. Akers *et al.*, Phys. Lett. **B337** (1994) 207.

- [8] ALEPH Collab., D. Buskulic *et al.*, Phys. Lett. **B373** (1996) 246;
DELPHI Collab., R. Keranen *et al.*, Phys. Lett. **B387** (1996) 651;
L3 Collab., M. Acciarri *et al.*, Phys. Lett. **B377** (1996) 289;
OPAL Collab., G. Alexander *et al.*, Z. Phys. **C73** (1997) 201.
- [9] OPAL Collab., K. Ackerstaff *et al.*, Phys. Lett. **B389** (1996) 197.
- [10] OPAL Collab., K. Ackerstaff *et al.*, Z. Phys. **C75** (1997) 409.
- [11] ALEPH Collab. B. Barate *et al.*, Phys. Lett. **B413** (1997) 431.
- [12] OPAL Collab., K. Ahmet *et al.*, Nucl. Instr. Meth. **A305** (1991) 275;
P.P. Allport *et al.*, Nucl. Instr. Meth. **A324** (1993) 34;
P.P. Allport *et al.*, Nucl. Instr. Meth. **A346** (1994) 476;
A. Honma *et al.*, Nucl. Instr. Meth. **A348** (1994) 409.
- [13] B.E. Anderson *et al.*, IEEE Trans. Nucl. Sci. **41** (1994) 845.
- [14] Eds. G. Altarelli, T. Sjöstrand and F. Zwirner, ‘Physics at LEP2’, CERN 96-01, vol. 2 (1996) 340.
- [15] T. Sjöstrand, Comp. Phys. Comm. **82** (1994) 74.
- [16] B. Andersson *et al.*, Phys. Rep. **97** (1983) 31.
- [17] OPAL Collab., G. Alexander *et al.*, Z. Phys. **C69** (1996) 543.
- [18] C. Peterson, D. Schlatter, I. Schmitt and P.M. Zerwas, Phys. Rev. **D27** (1983) 105.
- [19] M. Suzuki, Nucl. Phys. **B258** (1985) 553.
- [20] J. Allison *et al.*, Nucl. Instr. Meth. **A317** (1992) 47.
- [21] S. Jadach, B. F. L. Ward and Z. Wąs, Comp. Phys. Comm. **79** (1994) 503.
- [22] S. Jadach, W. Płaczek, and B.F.L. Ward, in ‘Physics at LEP2’, eds. G. Altarelli, T. Sjöstrand and F. Zwirner, CERN 96-01, vol. 2 (1996).
- [23] R. Engel and J. Ranft, Phys. Rev. **D54** (1996) 4244.
- [24] G. Marchesini *et al.*, Comp. Phys. Comm. **67** (1992) 465.
- [25] J.A.M. Vermaseren, Nucl. Phys. **B229** (1983) 347.
- [26] J. Fujimoto *et al.*, Comp. Phys. Comm. **100** (1997) 128.
- [27] S. Catani *et al.*, Phys. Lett. **B269** (1991) 432.
- [28] OPAL Collab., R. Akers *et al.*, Phys. Lett. **B327** (1994) 411;
OPAL Collab., R. Akers *et al.*, Z. Phys. **C65** (1994) 17.
- [29] OPAL Collab., P. Acton *et al.*, Z. Phys. **C58** (1993) 523;
OPAL Collab., R. Akers *et al.*, Z. Phys. **C60** (1993) 199.
- [30] Particle Data Group, Phys. Rev. **D54** (1996) 694.

- [31] M.G. Bowler, Z. Phys. **C11** (1981) 169.
- [32] R.D. Cousins and V.L. Highland, Nucl. Instr. Meth. **A320** (1992) 331.
- [33] F.A. Berends, R. Pittau, R. Kleiss, Comp. Phys. Comm. **85** (1995) 437.
- [34] L3 Collab., O. Adriani *et al.*, Phys. Rep. **236** (1993) 1;
ALEPH Collab., D. Decamp *et al.*, Phys. Rep. **216** (1992) 253.

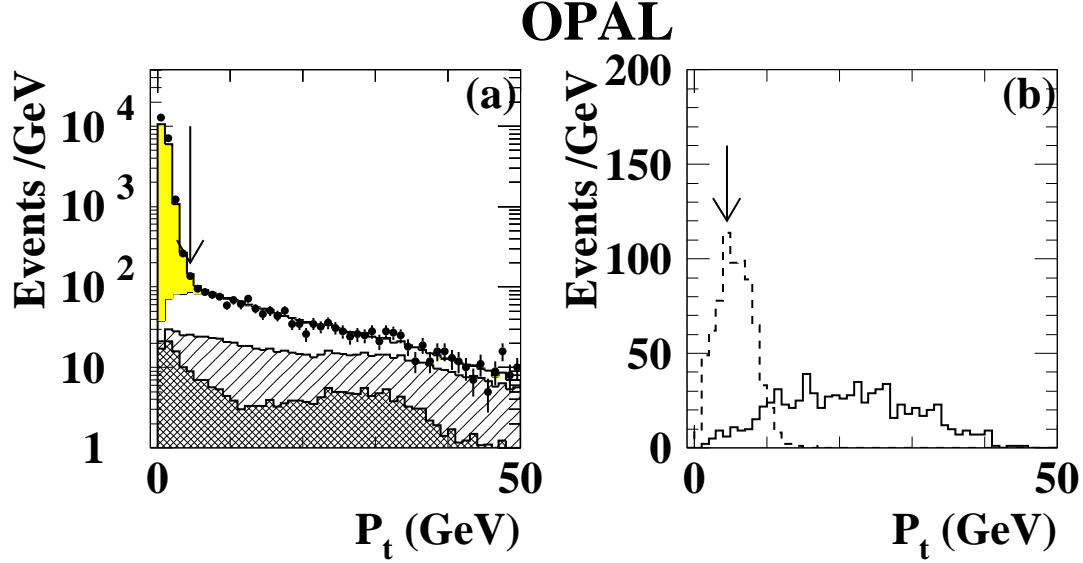


Figure 1: The distributions of P_t after cut (A1) for background (histograms) and data in (a), and for $\tilde{t}_1\tilde{t}_1^*$ predictions in (b). The arrows in these figures show the selection criteria. In (a) the distribution of the data is shown by the points with error bars. The predictions from background processes are also shown: dilepton events (cross-hatched area), two-photon processes (grey area), four-fermion processes (singly-hatched area), and multihadronic events (open area). (b) shows predictions for $\tilde{t}_1\tilde{t}_1^*$ in which \tilde{t}_1 decays into $c\tilde{\chi}_1^0$. The continuous line histogram is for $(m_{\tilde{t}_1}, m_{\tilde{\chi}_1^0}) = (80 \text{ GeV}, 60 \text{ GeV})$, and the dashed line is for $(80 \text{ GeV}, 75 \text{ GeV})$, starting from 1000 generated events each.

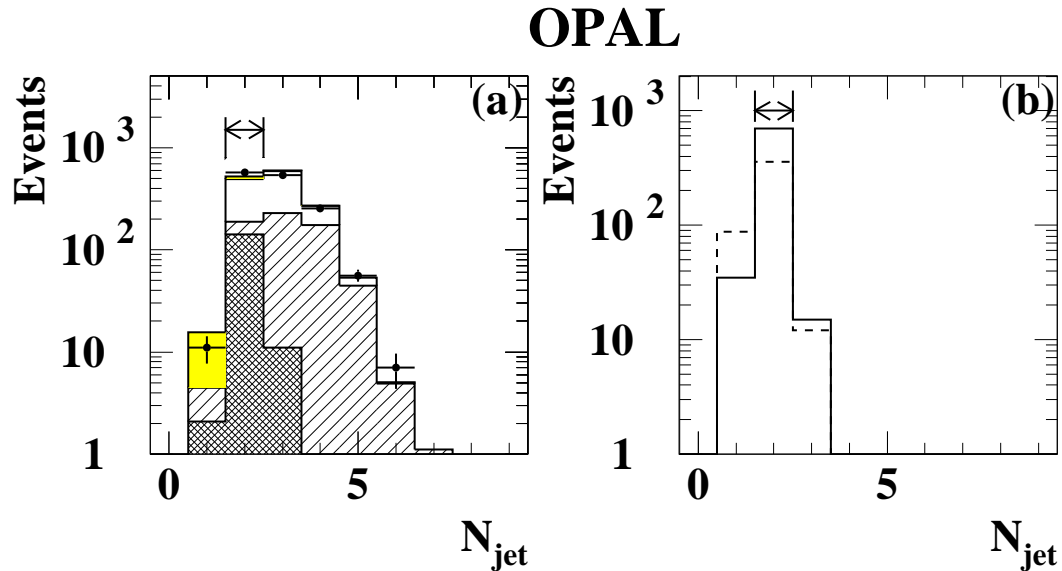


Figure 2: The distributions of the number of reconstructed jets after cut (A2): for background (histograms) and data in (a), and for $\tilde{t}_1\tilde{t}_1^*$ predictions in (b). The conventions for the various histograms are the same as in Fig. 1.

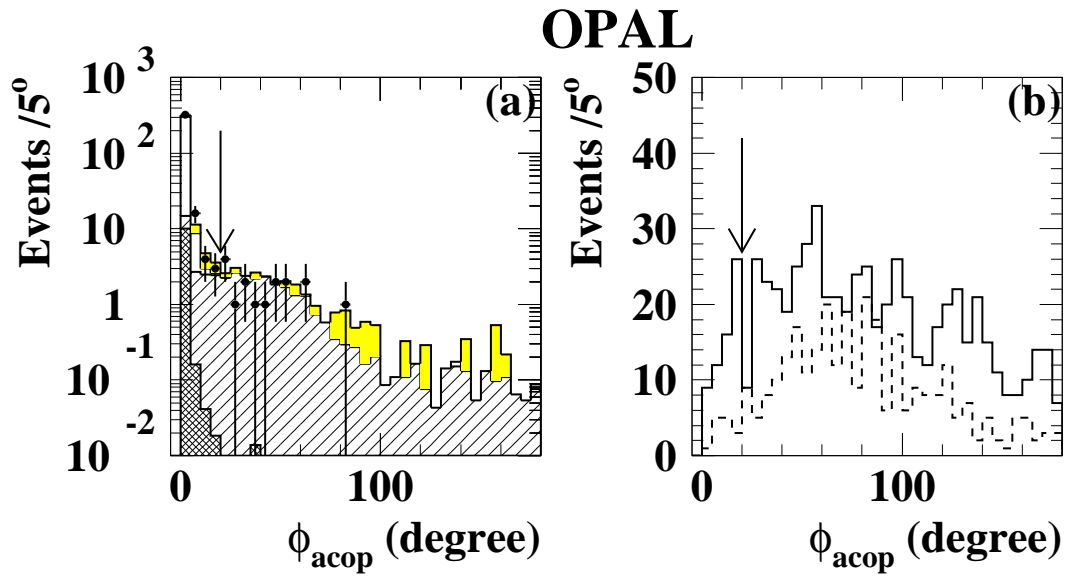


Figure 3: The distributions of the acoplanarity angle after cut (A3) for background (histograms) and data in (a), and for the $\tilde{t}_1\tilde{t}_1$ predictions in (b). The conventions for the various histograms are the same as in Fig. 1.

OPAL

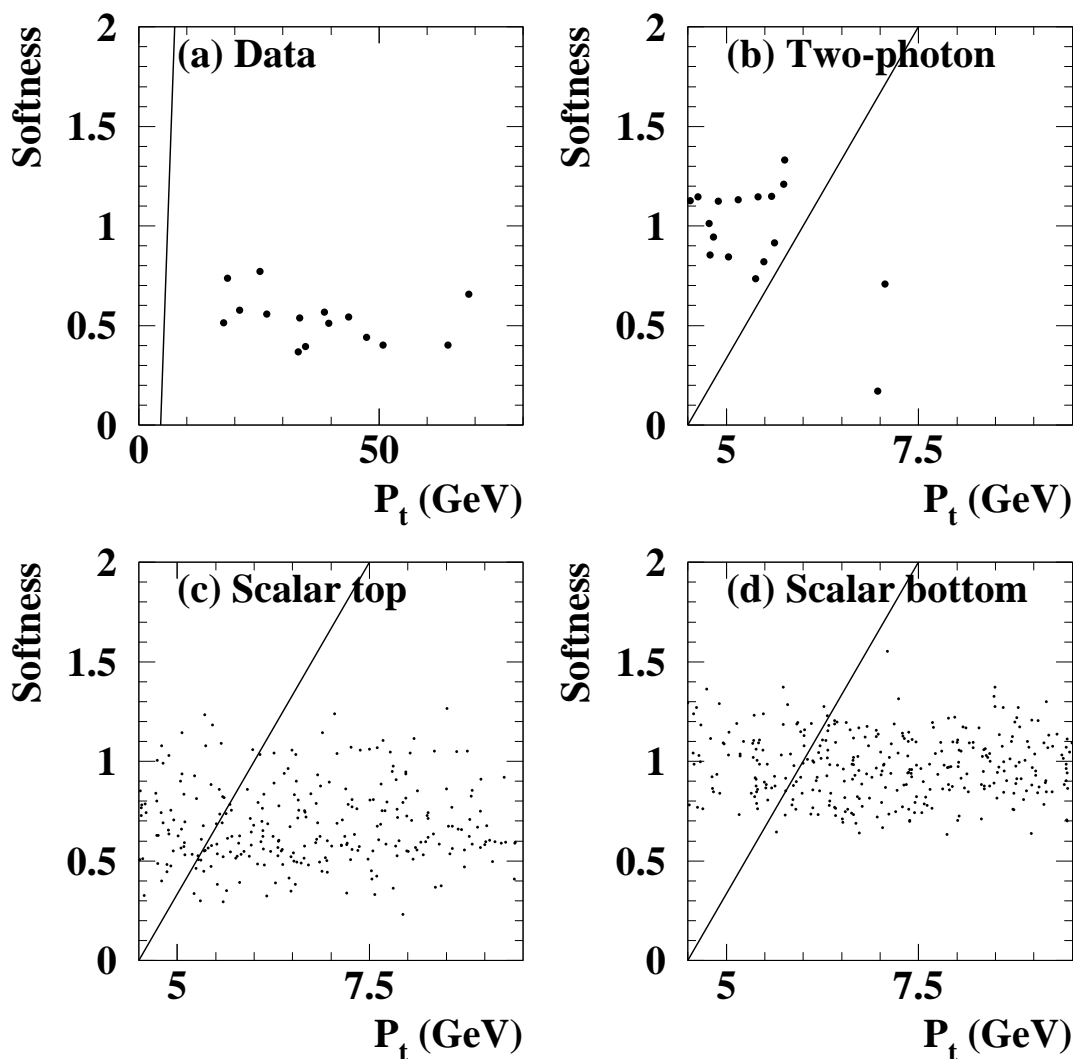


Figure 4: Scatter plots of ‘Softness’(see text) versus P_t after cut (A4) for (a) data, (b) simulated two-photon processes, (c) the Monte Carlo simulation of $\tilde{t}_1\tilde{\bar{t}}_1$ signals for $(m_{\tilde{t}_1}, m_{\tilde{\chi}_1^0}) = (80 \text{ GeV}, 75 \text{ GeV})$, and (d) the Monte Carlo simulation of $\tilde{b}_1\tilde{\bar{b}}_1$ signals for $(m_{\tilde{b}_1}, m_{\tilde{\chi}_1^0}) = (80 \text{ GeV}, 73 \text{ GeV})$. The scale of P_t in (a) is different from the other figures. The simulated events are not normalised to the luminosity. For the two-photon processes, the corresponding luminosity is 253 pb^{-1} . The event samples of $\tilde{t}_1\tilde{\bar{t}}_1$ and $\tilde{b}_1\tilde{\bar{b}}_1$ each start from 1000 events.

OPAL

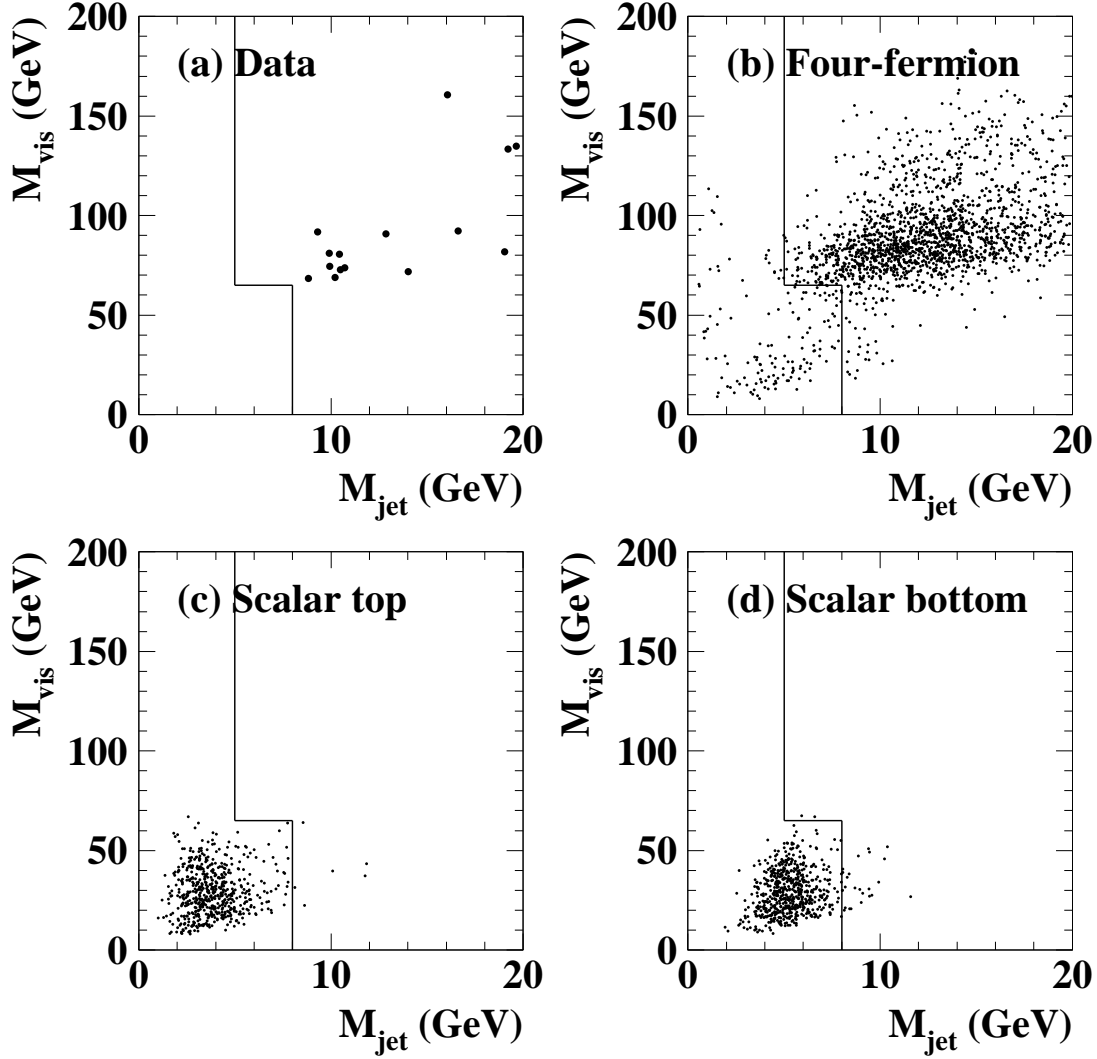


Figure 5: Scatter plots of M_{vis} versus \bar{M}_{jet} after cut (A5) for (a) data, (b) simulated four-fermion processes, (c) the Monte Carlo simulation of $\tilde{t}_1\bar{\tilde{t}}_1$ signals for $(m_{\tilde{t}_1}, m_{\tilde{\chi}_1^0}) = (80 \text{ GeV}, 60 \text{ GeV})$, and (d) the Monte Carlo simulation of $\tilde{b}_1\bar{\tilde{b}}_1$ signals for $(m_{\tilde{b}_1}, m_{\tilde{\chi}_1^0}) = (80 \text{ GeV}, 60 \text{ GeV})$. The simulated events are not normalised to the luminosity. For the four-fermion processes, the corresponding luminosity is 5000 pb^{-1} . The event samples of $\tilde{t}_1\bar{\tilde{t}}_1$ and $\tilde{b}_1\bar{\tilde{b}}_1$ each start from 1000 events.

OPAL

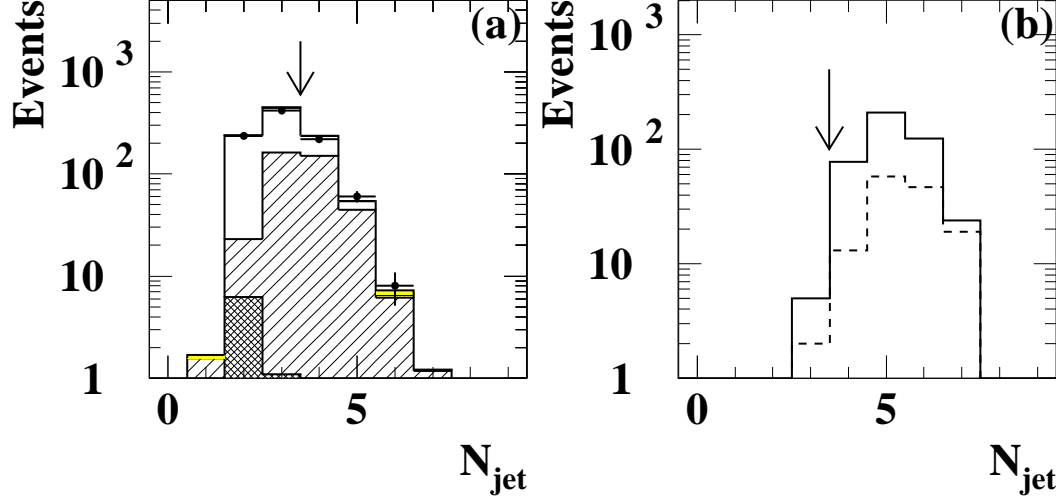


Figure 6: The distributions of the number of reconstructed jets after cut (B-L2). The arrows in these figures show the selection criteria. (a) shows the distribution of the data with error bars. The predictions from background processes are also shown: dilepton events (cross-hatched area), two-photon processes (grey area), four-fermion processes (singly-hatched area), and the multihadronic events (open area). (b) shows predictions for $\tilde{t}_1\tilde{t}_1^*$ in which \tilde{t}_1 decays into $b\ell\bar{\nu}$. The continuous line histogram is for $(m_{\tilde{t}_1}, m_{\bar{\nu}}) = (80 \text{ GeV}, 70 \text{ GeV})$, and the dotted line is for $(80 \text{ GeV}, 73 \text{ GeV})$. In these samples, the branching fraction to each lepton flavour is assumed to be the same.

OPAL

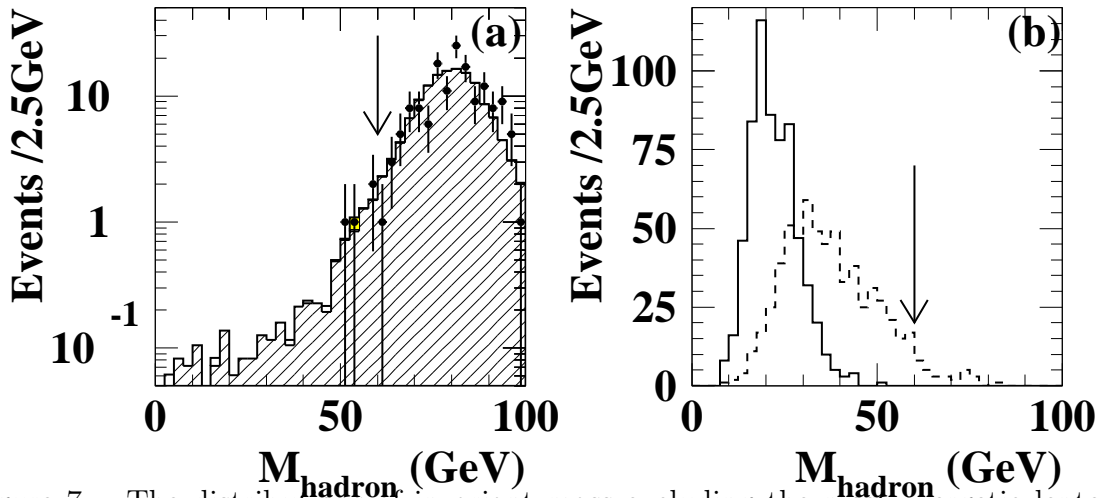


Figure 7: The distributions of invariant mass excluding the most energetic lepton after cut (B-H5). The arrows in these figures show the selection criteria. The conventions for the various histograms in (a) are the same as in Fig. 6. In (b) the continuous line histogram is for $(m_{\tilde{t}_1}, m_{\bar{\nu}}) = (80 \text{ GeV}, 60 \text{ GeV})$, and the dotted line is for $(80 \text{ GeV}, 40 \text{ GeV})$. In these samples, the branching fraction to each lepton flavour is assumed to be the same.

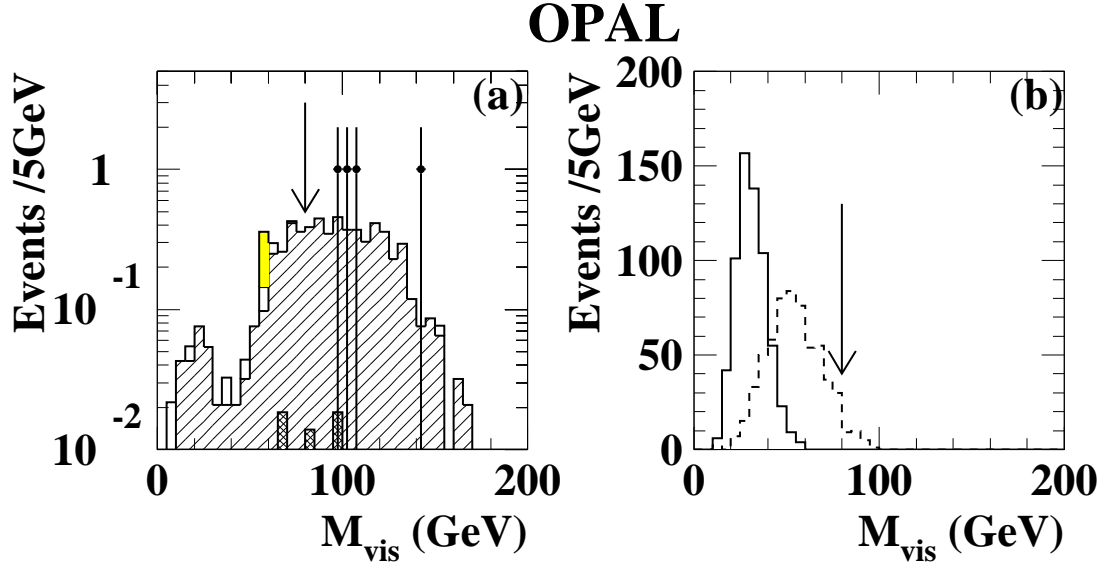


Figure 8: The distributions of the visible mass after cut (B-H6) for background (histograms) and data in (a), and for the $\tilde{t}_1\tilde{t}_1$ signal predictions in (b). The conventions for the various histograms are the same as in Fig. 7.

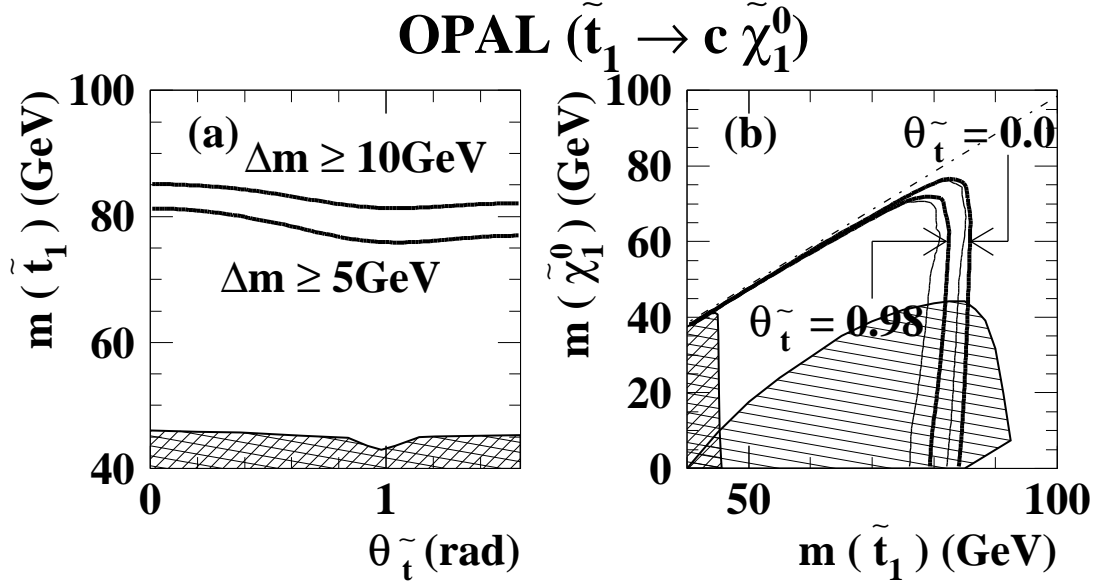


Figure 9: The 95% C.L. excluded regions assuming that the \tilde{t}_1 decays into $c\tilde{\chi}_1^0$. (a) The excluded regions in the $(\theta_{\tilde{t}}, m_{\tilde{t}_1})$ plane for a mass difference $\Delta m (= m_{\tilde{t}_1} - m_{\tilde{\chi}_1^0}) \geq 10$ GeV, and $\Delta m \geq 5$ GeV. The cross-hatched region has already been excluded by the search at LEP1 [7]. (b) The excluded regions in the $(m_{\tilde{t}_1}, m_{\tilde{\chi}_1^0})$ plane, for a mixing angle of \tilde{t}_1 of 0.0 and 0.98 rad. The solid lines show the actual limits, and the thin lines show the limits calculated only with the expected number of background events. The cross-hatched region has already been excluded by the search at LEP1 [7]. The singly-hatched region has been excluded by the D0 Collaboration [6]. The dash-dotted straight line shows the kinematic limit for the $\tilde{t}_1 \rightarrow c\tilde{\chi}_1^0$ decay.

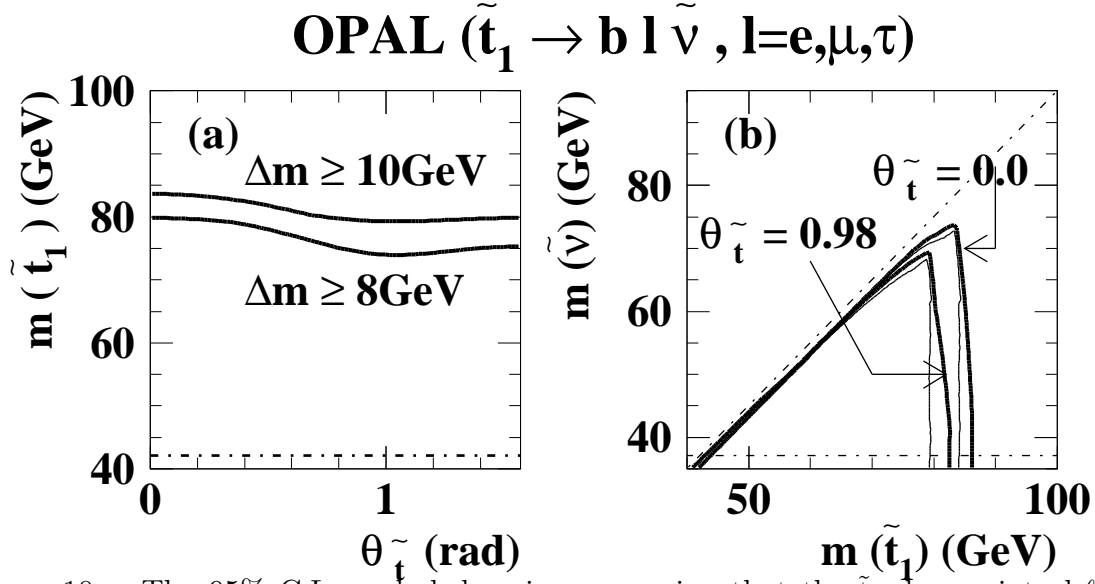


Figure 10: The 95% C.L. excluded regions assuming that the \tilde{t}_1 decays into $b\ell\tilde{\nu}$ and that the branching fraction to each lepton flavour is the same. (a) The excluded regions in the $(\theta_{\tilde{t}}, m_{\tilde{t}_1})$ plane where the mass difference between the \tilde{t}_1 and the $\tilde{\nu}$ is greater than 8 or 10 GeV. The dash-dotted straight line shows the kinematic limit for this decay, since a $\tilde{\nu}$ lighter than 37.1 GeV has been excluded [34, 30]. (b) The excluded regions in the $(m_{\tilde{t}_1}, m_{\tilde{\nu}})$ plane, for a mixing angle of the \tilde{t}_1 assumed to be 0.0 and 0.98 rad. The solid lines show the actual limits, and the thin lines show the limits calculated only with the expected number of background events. The dash-dotted horizontal line shows the limit on $m_{\tilde{\nu}}$ obtained at LEP1, and the dash-dotted diagonal line shows the kinematic limit for the $\tilde{t}_1 \rightarrow b\ell\tilde{\nu}$ decay.

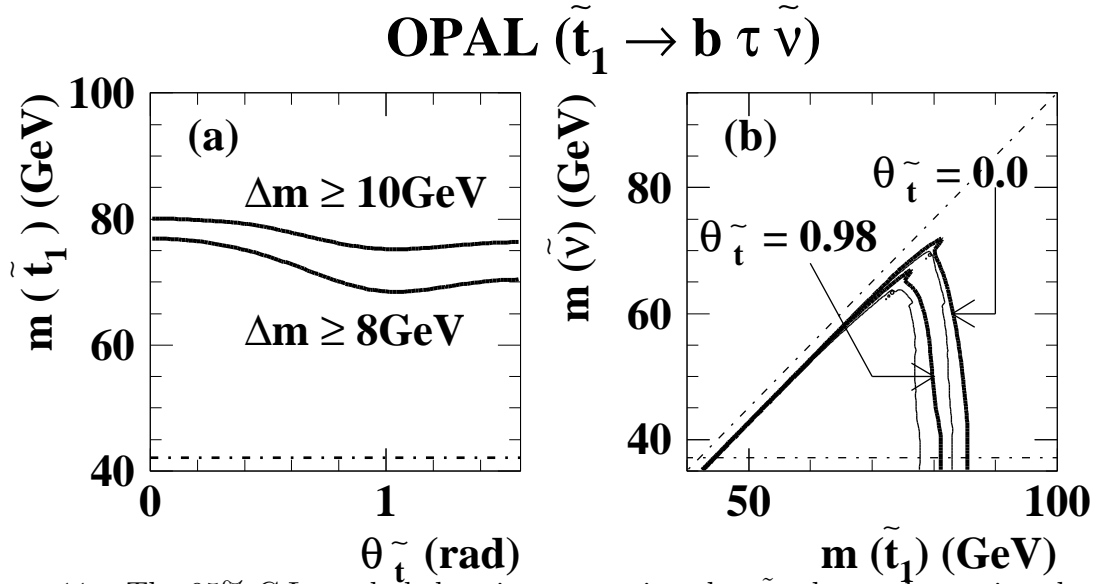


Figure 11: The 95% C.L. excluded regions assuming that \tilde{t}_1 always decays into $b\tau\tilde{\nu}_\tau$. (a) The excluded regions in the $(\theta_{\tilde{t}}, m_{\tilde{t}_1})$ plane where the mass difference between the \tilde{t}_1 and the $\tilde{\nu}_\tau$ is greater than 8 or 10 GeV. The dash-dotted straight line shows the kinematic limit for this decay. (b) The excluded regions in the $(m_{\tilde{t}_1}, m_{\tilde{\nu}})$ plane, for a mixing angle of the \tilde{t}_1 assumed to be 0.0 and 0.98 rad. The solid lines show the actual limits, and the thin lines show the limits calculated only with the expected number of background events. The dash-dotted horizontal line shows the limit on $m_{\tilde{\nu}}$ obtained at LEP1 [34, 30], and the dash-dotted diagonal line shows the kinematic limit for the $\tilde{t}_1 \rightarrow b\tau\tilde{\nu}$ decay.

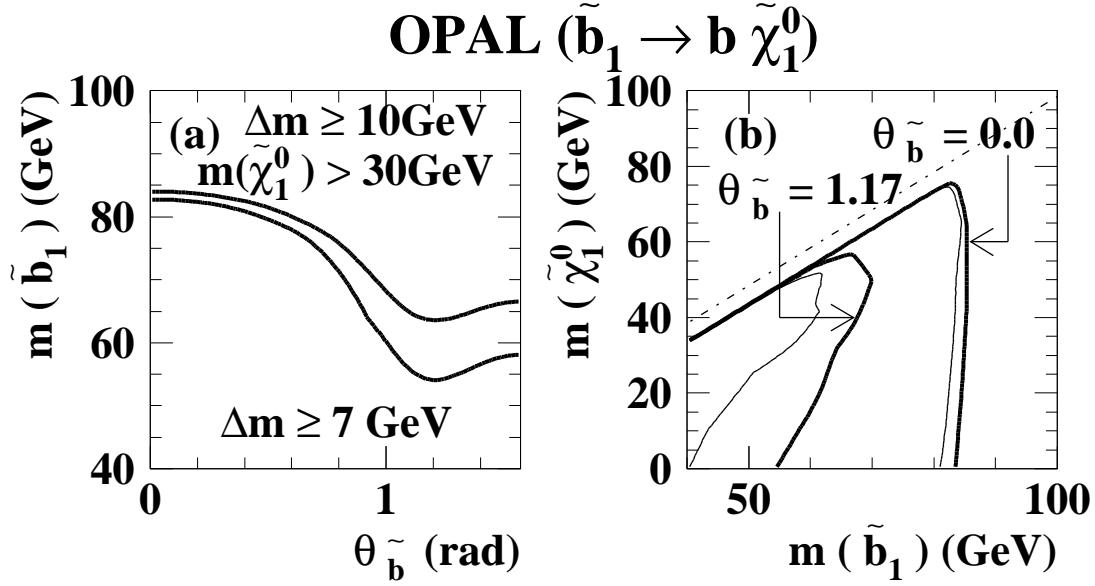


Figure 12: The 95% C.L. excluded regions assuming that the \tilde{b}_1 decays into $b\tilde{\chi}_1^0$.
(a) The excluded region in the $(\theta_{\tilde{b}}, m_{\tilde{b}_1})$ plane for a mass difference, $\Delta m (= m_{\tilde{b}_1} - m_{\tilde{\chi}_1^0})$, $\Delta m \geq 10 \text{ GeV}$ and $\tilde{\chi}_1^0$ is heavier than 30 GeV. The excluded region for $\Delta m \geq 7 \text{ GeV}$ is also shown.
(b) The excluded regions in the $(m_{\tilde{b}_1}, m_{\tilde{\chi}_1^0})$ plane, for a mixing angle of the \tilde{b}_1 assumed to be 0.0 and 1.17 rad. The solid lines show the actual limits, and the thin lines show the limits calculated only with the expected number of background events.

